POLITECNICO DI TORINO

Corso di Laurea Magistrale

in Ingegneria Aerospaziale e Astronautica

Tesi di Laurea Magistrale

Debris Removal via Tethered Space-Tug System

Relatori

prof. Qi Rui

prof. Lorenzo Casalino

Candidato

Enrico Congiu

Anno Accademico 2018/2019

1 SUMMARY

Figure index:

2 PURPOSE OF THE STUDY

This study has been developed to analyse the dynamics of the debris and the entire Tethered Space System during debris recovery operations using a tether with a tape geometry and in case of low thrust of the space tug. The work is divided in five chapters. The introduction chapter gives a description of the current situation of Earth's near space in terms of presence of space debris and debris mitigation initiatives. Also in this part there is a description of the roles of tethers in debris' mitigation efforts and how it is possible to study their behaviour in space. The mathematical model chapter describes the mathematical model used to study the dynamics of the Tethered Space System, which consist on the equations of motion of the system bodies and a description of the tether's model used. The chapter dedicated to the studied cases explains what configurations and what starting conditions of the Tethered Space System have been used, and in the results chapter there is a description of the results obtained. The conclusion chapter sums up the results obtained in all the work.

3 INTRODUCTION:

Since the beginning of space exploration the number of debris in earth orbit and beyond has started to rise. Spent stages, old satellites, fragments produced by explosion and collisions, even a glove, constitute the population of debris around earth. Such a cloud of debris poses a threat for current and future space missions, and rises security concerns for long time manned space missions. At the moment [1] there are in earth orbit: 34000 objects larger than 10 cm, 900000 objects between 1 cm to 10 cm and 128 million objects between 1 mm to 1 cm. This scenario is going to evolve over time with an increase of space debris as new satellite launches take place and as collisions between debris and satellite will occur.

One strategy to limit the increase of space debris production for every new space mission, consists of a series of operations to be applied as the satellite reaches the End of Life (EoL), which go under the name of Post Mission Disposal strategies (PMD). They consist of different operations such as: battery passivation, residual fuel dumping, transfer to a graveyard orbit or deorbiting of the satellite in 25 years' time [2].
Without PMD strategies it is expected an increase of 330% of the debris' population larger than 10 cm in the next 200 years [3], but even with PMD strategies applied in every mission and with no more space launches it is predicted that the debris population will increase [4].

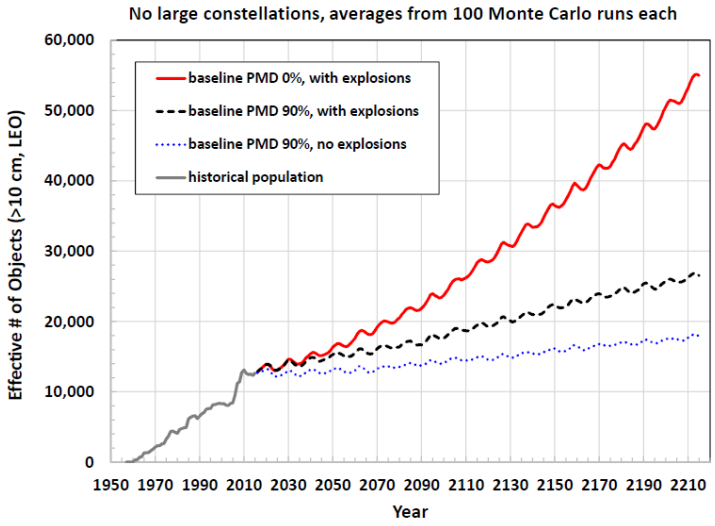

Figure 1: Simulated historical LEO environment and results from three different future projection scenarios

For this reason, ESA has started a Clean Space Initiative with the aim of reducing the debris' population. It consists in applying PMD strategies to all current and future space missions and in another initiative called Active Debris Removal with the purpose of deorbiting from 5 to 10 big satellites per year. The choice of the objects to be disposed follows this criteria:

- High mass of the object;
- High probability of collision in the near future;
- High altitude orbit.

A first step of the Active Debris Removal initiative has been the demonstration of the feasibility of the debris capture operations. With this scope, the RemoveDEBRIS mission has proven the feasibility of the debris capture using a tether and a harpoon. The next step will be the mission e.deorbit planned for 2023 with the aim of deorbiting an observation satellite.

The link between the active satellite and the debris is usually achieved using a tether. This configuration has the name of Tethered Satellite System (TSS). Tethers have several advantages (very low weight) and

disadvantages (low stiffness and damping). For this reason, there is a great interest in using tether devices in space, but it is still a challenge to accurately predict the motion of a TSS during orbital operations.

Tethers can be used not only to connect two objects, but also: to provide thrust, to produce electricity, to stabilize a spacecraft without using fuel, etc. These features have led to a series of tests in space, such as TSS-1R, YES, Charge-1, Charge-2, T-Rex, which have tested the capabilities of electricity production, electrodynamic tether propulsion and have produced a considerable amount of data on the dynamic behaviour of tethers in space.

Several forces influence the dynamic of tethers during operations:

- Gravity forces: they cause a torque that tends to align the system along the radius vector of the system. This torque is the reason why tethers have a great use in spacecraft stabilization;
- Solar Pressure forces: they are the result of the interaction of the surface tether with the sunlight. It depends on the shape of the tether and on the reflectivity of its surface;
- Electrodynamic forces: they result from the interaction of the plasma environment in the ionosphere and earth's magnetic field. They have fundamental implications for power generation and spacecraft propulsion;
- Atmospheric drag: it is exploited to lower the orbit of a satellite just by increasing the drag of the system;

Depending on the configuration of the tether, the impact of these forces varies. For example, a long tether will be more sensitive to the gravity gradient forces compared to a short one, and a bare tether will feel a stronger electrodynamic force compared to an insulated one since the electron collection efficiency is much lower for the latter [5].

The combination of this forces generates a chaotic motion of the TSS and the use of control systems may be fundamental to limit over range motions, as described by Zhongyi et al [6].

It has been observed that for certain conditions of low thrust, the TSS can oscillate between two configurations of the system even if the system does provide damping of the motion [7]. These oscillations, if not controlled, can lead to high stress in the tether and also to entanglement. Such scenarios should be avoided to make sure the tether does not break up.

At this moment two main tether configurations are studied, the string tether and the tape tether. The string tether has a cylindrical shape and it is flexible in every direction, while the tape tether is thin and wide, so it is flexible only in one direction. The string tether configuration has been already tested several times in space while the tape tether is gaining interest just in recent years, especially after T-Rex test developed by ISAS/JAXA.

String tethers have a more predictable behaviour compared to tape tethers, but on the other hand tape tethers do provide a better survivability against micro-meteoroids impacts as reported by Shaker Bayajid Khan [8], where for long periods in LEO the fatal impacts frequency is between 42 to 54 times higher for string tethers compared to tape tethers. Also tape tethers have a better efficiency in electron collection processes, so they are more suitable for electrodynamic applications.

There are several models available for the study of a Tethered Space System [9]:

- Dumbbell model: in this model the tether is assumed as massless and the flexibility effects are ignored;
- Spring-damper model: in this method the tether is modelled as a series of elements, where each one of them is a combination of a spring and a damper. This method has unfortunately the disadvantage of requiring a big number of elements to calculate big deformations of the tether.
- Finite Elements Method:
    - Nodal position finite element method;

- Absolute Nodal Coordinate Formulation: developed by Shabana [10], this model derives from the class of finite elements methods, and it is well suitable to analyse large deformations, when the non-linear behaviour of the tether cannot be ignored.

For the analysis in this paper a tape tether with spring-damper model will be used to simulate the motion of the TSS during towing operations.

4 MATHEMATICAL MODEL:

The Tether Space System has been modelled using Newtonian mechanics, so for each element we have a set of six differential equations, three for translation in the Cartesian system x-y-z and three for rotation around the Cartesian axes x-y-z. In order to perform the analyses, three categories of reference frames have been used:

- Earth Centred Inertial frame (ECI): referred with the subscript "i";
- Local Vertical-Local Horizontal (LVLH) frame: this reference frame has the origin in the centre of mass of the system, where the x axis coincides with the orbital radius vector of the system's centre of mass and the z axis is perpendicular to the orbital plane and points in the same direction of the orbital angular momentum vector $\bar{h}$. The y axis follows the right hand rule. We will refer to this frame of reference using the subscript "o".
- Local body frame of reference: this frame of reference is specific for each body analysed. It provides an indication of the attitude of the body and it is centred in the centre of mass of the body itself. The subscripts for the bodies' frame of reference analysed are:
    - Space tug: "1";
    - Space debris: "2";
    - Tether elements: "e";

The orbit of the system is described by six orbital parameters:

- p: is the "semilatus rectum";
- e: is the orbit eccentricity;
- i: is the orbital plane inclination;
- ω: is the argument of the periapsis;
- Ω: is the longitude of the ascending node;
- θ: is the true anomaly;

The system's centre of mass trajectory has been described using the Modified Equinoctial Parameters [11]:

$$\begin{cases} \dfrac{dp}{dt} = \dfrac{2p}{w}\sqrt{\dfrac{p}{\mu}}a_y \\ \dfrac{df}{dt} = \sqrt{\dfrac{p}{\mu}}\left\{a_x sinL + [(w+1)cosL + f]\dfrac{a_y}{w} - (hsinL - kcosL)\dfrac{g a_z}{w}\right\} \\ \dfrac{dg}{dt} = \sqrt{\dfrac{p}{\mu}}\left\{-a_x cosL + [(w+1)sinL + g]\dfrac{a_y}{w} + (hsinL - kcosL)\dfrac{f a_z}{w}\right\} \\ \dfrac{dh}{dt} = \sqrt{\dfrac{p}{\mu}}\dfrac{s^2 a_z}{2w}cosL \\ \dfrac{dk}{dt} = \sqrt{\dfrac{p}{\mu}}\dfrac{s^2 a_z}{2w}sinL \\ \dfrac{dL}{dt} = \dfrac{w^2}{p^2}\sqrt{\mu p} + \dfrac{1}{w}\sqrt{\dfrac{p}{\mu}}(hsinL - kcosL)a_z \end{cases} \quad (1)$$

where:

$$w = 1 + fcosL + gsinL; \quad (2)$$

$$s^2 = 1 + h^2 + k^2; \quad (3)$$

$$a_x = 0;\ a_y = \frac{F}{m_1 + m_2 + m_t};\ a_z = 0; \quad (4)$$

The instantaneous values of position, angular velocity and angular acceleration of the centre of mass are:

$$R_o = \frac{p}{w}; \quad (5)$$

$$\omega_o = \frac{w^2}{p^2}\sqrt{\mu p}; \quad (6)$$

$$\epsilon_o = \frac{-2\omega_o}{w}(fsinL - gcosL); \quad (7)$$

These equations are integrated together with the equations of motion of each body.

The system is composed of N+2 bodies, where N is the number of rigid elements used to describe the motion of the tether, while the other two are the debris and the space tug. To describe the motion of each element six equilibrium equations have to be solved, three for translation and three for rotation of the body. The purpose of the analysis is to analyse the variations of the debris angle θ and the libration angle α, as shown in Figure 2 and Figure 3. Figure 4 shows how the inclination of the tether segment β is measured relative to the orbital plane.

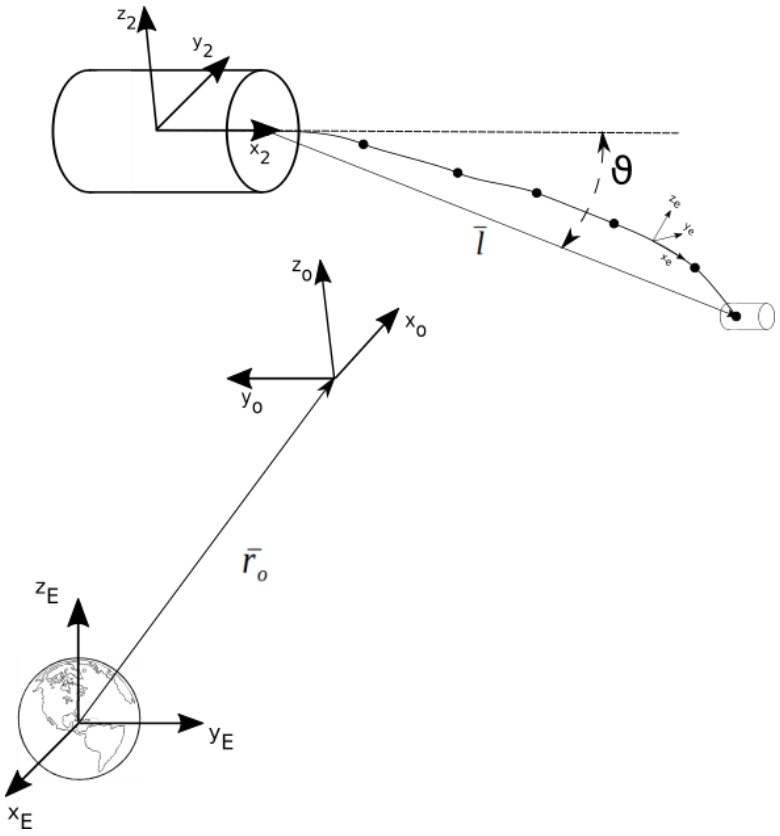

Figure 2: Tether Space System schematic

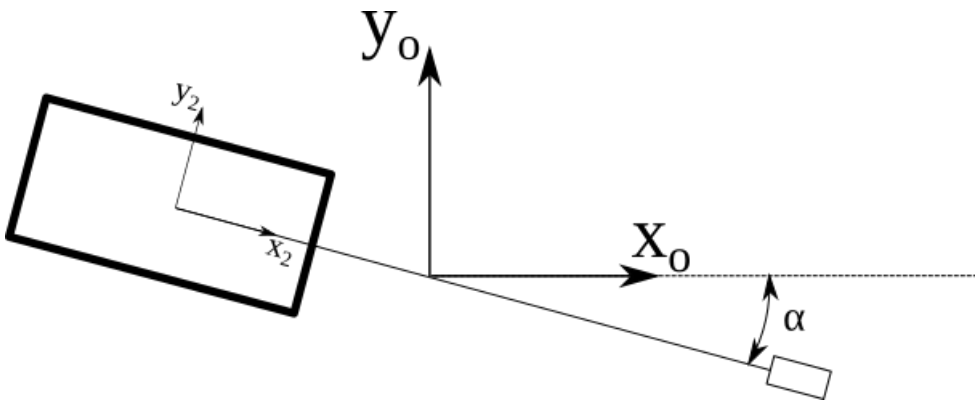

Figure 3: α measurement

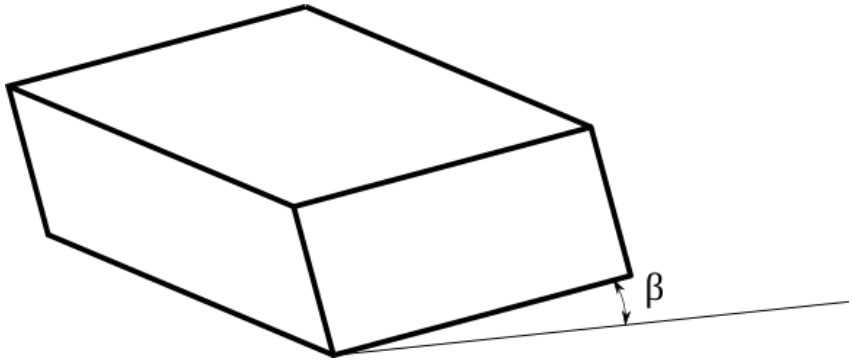

Figure 4: β measurement

4.1 SPACE DEBRIS AND SPACE TUG MODEL:

4.1.1 Translational motion:

Debris' and tug's translation equilibrium is described by vector equations:

$$m_1\bar{a}_1 = [A^{io}](m_1\bar{g}_1 + \bar{T}_1 + \bar{F} + \bar{D}_1) \quad (8)$$

$$m_2\bar{a}_2 = [A^{io}](m_2\bar{g}_2 + \bar{T}_2 + \bar{D}_2) \quad (9)$$

where:

- m_1 is the mass of the space tug;
- m_2 is the mass of the space debris;
- $\bar{a}_1$ and $\bar{a}_2$ are the accelerations of the space tug and space debris measured in the ECI frame;
- $[A^{io}]$ is the rotation matrix which transforms vectors expressed in the LVLH frame in the ECI frame;
- $\bar{g}_1$ and $\bar{g}_2$ are the gravitational accelerations applied on the space tug and the space debris;
- $\bar{T}_1$ and $\bar{T}_2$ are the tether forces applied to the debris and the tug;
- $\bar{F}$ is the force provided by the tug's thruster;
- $\bar{D}$ is the atmospheric drag;

The rotation matrix $[A^{io}]$ is defined as:

$$[A^{io}] = \begin{Bmatrix} c_\Omega c_{\omega+\theta} - c_i s_\Omega s_{\omega+\theta} & -c_i s_\Omega c_{\omega+\theta} - c_\Omega s_{\omega+\theta} & s_i s_\Omega \\ c_i c_\Omega s_{\omega+\theta} + s_\Omega c_{\omega+\theta} & c_i c_\Omega c_{\omega+\theta} - s_\Omega s_{\omega+\theta} & -s_i c_\Omega \\ s_i s_{\omega+\theta} & s_i c_{\omega+\theta} & c_i \end{Bmatrix} \quad (10)$$

where: $c_\Omega = cos(\Omega);\ s_\Omega = sin(\Omega);\ c_i = cos(i);\ s_i = sin(i);\ c_{\omega+\theta} = cos(\omega+\theta);\ s_{\omega+\theta} = sin(\omega+\theta);$

The acceleration provided by gravity is:

$$\bar{g}_j = -\mu \frac{\bar{r}_j}{\left|\bar{r}_j\right|^3},\ j = 1,2. \tag{11}$$

where $\bar{r}_j$ is the position vector of the body relative to the ECI frame.

Forces $\bar{T}_1$ and $\bar{T}_2$ are provided by the mathematical model which describes the tether motion, while the thrust force $\bar{F}$ is constant.

The atmospheric drag is described by the equation:

$$\bar{D} = -\frac{1}{2}\rho c_D S_\perp |\bar{V}_{rel}|\bar{V}_{rel} \tag{12}$$

Where:

- ρ is the atmosphere density provided by the Jacchia model [12] and is a function of the flight altitude;
- c_D is the drag coefficient;
- $S_\perp$ is the front section of the body invested by the stream of gas;
- $\bar{V}_{rel}$ is the relative velocity between the body and the atmosphere, which for simplicity has been supposed to have the same angular motion of earth;

4.1.2 Rotational motion:

For simplicity it has been imposed that the space tug does not rotate during the simulation, in fact it has been assumed that the spacecraft should be able to maintain a specific orientation using the Attitude Determination and Control System (ADCS). With this hypothesis, only the attitude of the debris has been analysed.

The rotation of the debris is described by Euler equation:

$$[J_2]\dot{\bar{\omega}}_2 + \bar{\omega}_2 \times [J_2]\bar{\omega}_2 = \bar{M}_2 \tag{12}$$

Where:

- $[J_2]$ is the inertia matrix of the debris. Since the debris has been assumed as a cylinder with homogeneous mass distribution, the matrix is diagonal. The matrix is in the form:

$$[J_2] = \begin{bmatrix} J_{xx} & 0 & 0 \\ 0 & J_{yy} & 0 \\ 0 & 0 & J_{zz} \end{bmatrix} \quad (13)$$

- $\dot{\bar{\omega}}_2$ and $\bar{\omega}_2$ are respectively the debris' absolute angular acceleration and absolute angular velocity;
- $\bar{M}_2$ is the sum of the torques applied on the body. It is defined as:

$$\bar{M}_2 = \bar{M}_t + \bar{M}_g \quad (14)$$

where $\bar{M}_t$ is the torque applied by the tether and $\bar{M}_g$ is the gravity gradient torque. $\bar{M}_t$ varies depending on the model of the tether assumed. In the simple case of the string tether model the torque is expressed as:

$$\bar{M}_t = \bar{\rho} \times \bar{T}_2 \quad (15)$$

where $\bar{\rho}$ is the vector of the attachment point. In the case of tape tether model, the torque applied by the tether on the debris will be described in the next section.

The gravity gradient torque is defined as:

$$\bar{M}_g = \frac{3\mu}{|\bar{r_2}|^3} \begin{bmatrix} (J_{zz} - J_{yy})\gamma_z\gamma_y \\ (J_{xx} - J_{zz})\gamma_z\gamma_x \\ (J_{yy} - J_{xx})\gamma_x\gamma_y \end{bmatrix} \quad (16)$$

where γ_x, γ_y and γ_z are the direction cosine between the axes of the debris' frame of reference and the position vector $\bar{r_2}$ measured in the ECI frame. These direction cosines are defined as:

$$\gamma_x = \frac{\bar{r_2}[A_1^{o2}]}{|\bar{r_2}|}, \ \gamma_x = \frac{\bar{r_2}[A_2^{o2}]}{|\bar{r_2}|}, \ \gamma_x = \frac{\bar{r_2}[A_3^{o2}]}{|\bar{r_2}|} \quad (17)$$

where $\left[A_j^{o2}\right]$ represents the j-th column of the direction cosine matrix of the debris.

The integration of the Euler equation (12) allows us to calculate the angular velocity of the debris. However in order to determine the attitude of the debris we should integrate the variation of the direction cosine matrix $[A^{o2}]$ that expresses the coordinates in the debris frame of reference into the LVLH frame.

This work is done by integrating the equation:

$$\frac{d[A^{o2}]}{dt} = -[\tilde{\Omega}_2][A^{o2}] \tag{18}$$

where:

$$[\tilde{\Omega}_2] = \begin{bmatrix} 0 & -\Omega_{2z} & \Omega_{2y} \\ \Omega_{2z} & 0 & -\Omega_{2x} \\ -\Omega_{2y} & \Omega_{2x} & 0 \end{bmatrix} \tag{19}$$

and:

$$\bar{\Omega}_2 = \bar{\omega}_2 - \bar{\omega}_o \tag{20}$$

$\bar{\Omega}_2$ represents the angular velocity of the debris with respect to the LVLH frame, while $\bar{\omega}_o$ is the angular velocity of the LHLV frame with respect to the ECI frame.

4.2 TETHER MODEL:

In this model, derived from the work of Yu et al [13], the tether is assumed as a series of rigid bodies connected to each one trough elastic joints. Joints are modelled as springs and dampers, so that each one can provide a torque if there is a deflection angle between two rigid bodies and a force if a displacement between the ends of two rigid bodies is present. Such visco-elastic joints also provide damping in order to simulate the hysteresis of the tether material during elastic deformation.

Each element is denoted by the "j" subscript and each one is counted starting from the element connected to the space tug up to the space debris. So the element connected to the space tug is the element j=1, while the element connected to the space debris is the element j=n.

Each rigid body element has a local reference frame and, since the tether is a tape, the three geometrical characteristics: length, width and thickness describe its geometry. The frame of reference is centred in the centre of mass of the element and the x axis seats along the length of the element. The x axis points toward the (j-1) element, the z axis is perpendicular to the plane of the element and the y axis completes the system following the third hand rule.

4.2.1 Loads applied to the elements:

Forces exchanged between joints follow the Kelvin–Voigt law:

$$\bar{P}_{j,m1} = K\bar{\eta}_{j,j-1} - D\dot{\bar{\eta}}_{j,j-1} \quad \text{and} \quad \bar{P}_{j,p1} = K\bar{\eta}_{j,j+1} - D\dot{\bar{\eta}}_{j,j+1} \tag{21,22}$$

K represents the stiffness of the element expressed as:

$$K = EA \tag{23}$$

And D is the tether damping:

$$D = EA\alpha_t^p \tag{24}$$

Where E is the Young modulus, A is the cross section and L_e is the element length.

The deformation $\bar{\eta}$ and the deformation speed $\dot{\bar{\eta}}$ are expressed as:

$$\dot{\bar{\eta}}_{j,j-1} = \frac{d}{dt}\left(\frac{dr_{j-1,j}}{dL}\right) \approx \frac{\left(\dot{\bar{r}}_{j-1,p1} - \dot{\bar{r}}_{j,m1}\right)}{L_e} \;,\; \dot{\bar{\eta}}_{j,j+1} = \frac{d}{dt}\left(\frac{dr_{j+1,j}}{dL}\right) \approx \frac{\left(\dot{\bar{r}}_{j-1,m1} - \dot{\bar{r}}_{j,p1}\right)}{L_e} \tag{25,26}$$

$$\bar{\eta}_{j,j-1} = \frac{dr_{j,j-1}}{dL} \approx \frac{\left(\bar{r}_{j-1,p1} - \bar{r}_{j,m1}\right)}{L_e} \;,\; \bar{\eta}_{j,j+1} = \frac{dr_{j,j+1}}{dL} \approx \frac{\left(\bar{r}_{j-1,m1} - \bar{r}_{j,p1}\right)}{L_e} \tag{27,28}$$

The first subscript indicates the element. The second subscript p1 indicates the end connected to the element j+1 while the subscript m1 indicates the end connected to the element j-1.

The terms $\bar{r}$ and $\dot{\bar{r}}$ in equations 25-28 represent the position and the velocity of the ends of each element.

On each element the force acting on its centre of mass due to the displacement of the nodes is equal to:

$$\bar{P}_j = \bar{P}_{j,m1} + \bar{P}_{j,p1} \tag{29}$$

The two forces acting on each element do provide a torque since they are not applied in the centre of mass of the element. The torque applied at each element is:

$$\bar{M}_j^p = \bar{\rho}_{j,m1} \times \bar{P}_{j,m1} + \bar{\rho}_{j,p1} \times \bar{P}_{j,p1} \tag{30}$$

where $\bar{\rho}_{j,m1}$ and $\bar{\rho}_{j,p1}$ represent the position vectors of the elements' extremities calculated from the centre of mass of the element itself.

Another load applied to each element is the gravitational force. This has the same formulation of equation (11):

$$\bar{g}_j = -\mu \frac{\bar{r}_j}{\left|\bar{r}_j\right|^3},\ j = 1,2,\dots,n \tag{31}$$

The last force acting on the tether segments is the aerodynamic drag, which follows the equation:

$$\bar{D}_j = -\frac{1}{2}\rho c_D S_{j,\perp} \left|\bar{V}_{j,rel}\right| \bar{V}_{j,rel} \tag{32}$$

Earth's gravity provides a torque to each element as described as in the equation (16):

$$\bar{M}_{j,g} = \frac{3\mu}{\left|\bar{r}_j\right|^3} \begin{bmatrix} (J_{j,zz} - J_{j,yy})\gamma_{j,z}\gamma_{j,y} \\ (J_{j,xx} - J_{j,zz})\gamma_{j,z}\gamma_{j,x} \\ (J_{j,yy} - J_{j,xx})\gamma_{j,x}\gamma_{j,y} \end{bmatrix} \ j = 1,2,\dots,n \tag{33}$$

The tape tether has two features, torsional and bending stiffness, that distinguish it from the string tether. Since the thickness of the tape tether is very small compared to its width, the bending stiffness related to the thickness of the tether has been considered negligible.

The bending torque is described by the equation:

$$\bar{M}_{j,k}^{b} = EI_z\left(\psi_{j,k}^{'} + \alpha_t^b \dot{\psi}_{j,k}^{'}\right)cos\left(\phi_{j,k}\right) \tag{34}$$

Terms $\psi_{j,k}^{'}$ and $\dot{\psi}_{j,k}^{'}$ represent respectively the bending deformation and deformation speed between the elements "j" and "j-1" but also between the elements "j" and "j+1" as described in the equations:

$$\psi_{j,k}^{'} = \frac{d\psi_{j,k}^{z}}{dL_e} \approx \frac{\psi_j^z - \psi_k^z}{L_e} \tag{35}$$

$$\dot{\psi}_{j,k}^{'} = \frac{d\dot{\psi}^{z}{}_{j,k}}{dL_e} \approx \frac{\dot{\psi}_j^z - \dot{\psi}_k^z}{L_e} \tag{36}$$

Where the terms $\psi_{j,k}^{z}$ and $\dot{\psi}^{z}{}_{j,k}$ represent respectively the relative angle and the relative angular velocity between elements "j" and "k". The term E is the Young modulus, I_z is the inertia stiffness of the tape, α_t^b is the damping coefficient. $\phi_{j,k}$ is the torsional angle between elements "j" and "k".

In total the bending torque applied to each element is:

$$\bar{M}_j^b = \bar{M}_{j,j-1}^b + \bar{M}_{j,j+1}^b \tag{37}$$

Torsional torque follows the Kelvin–Voigt law like the previous forces:

$$\bar{M}_{j,k}^{t} = GI_t\left(\phi_{j,k}^{'} + \alpha_t^t \dot{\phi}_{j,k}^{'}\right) \tag{38}$$

where:

$$\phi_{j,k}^{'} = \frac{d\phi_{j,k}}{dL_e} \approx \frac{\phi_j - \phi_k}{L_e} \tag{39}$$

$$\dot{\phi}_{j,k}^{'} = \frac{d\dot{\phi}_{j,k}}{dL_e} \approx \frac{\dot{\phi}_j - \dot{\phi}_k}{L_e} \tag{40}$$

G is the torsional modulus, $I_t$is the inertia torsional stiffness and α_t^t is the damping coefficient. In total the torsional torque applied to each element is:

$$\bar{M}_j^t = \bar{M}_{j,j-1}^t + \bar{M}_{j,j+1}^t \tag{41}$$

The torque exchanged from the tether to the space debris is:

$$\bar{M}_2 = \bar{M}^t_{j,j+1} + \bar{M}^b_{j,j+1} \tag{42}$$

The loads applied to each element are integrated in the following equations which follow the same solving method applied to the debris dynamics:

$$m_j \bar{a}_j = \left[A^{ij}\right]\left(m_j \bar{g}_j + \bar{P}_j + \bar{D}_j\right) \tag{43}$$

$$\left[J_j\right]\dot{\bar{\omega}}_j + \bar{\omega}_j \times \left[J_j\right]\bar{\omega}_j = \bar{M}_j \tag{44}$$

All equations have been implemented on MATLAB® with the use of the "ode15s" solver.

5 STUDIED CASES:

Five different tether configurations have been analysed to understand the behaviour of the tape tether:

1. The first configuration consists of a string tether of the same cross sectional area of the tape tether, but without any torsional nor bending stiffness. The string tether is free to bend and twist. It does not exchange any torque with the debris and the space tug. The tether does not damp the bending motion.
2. In the second configuration a tape tether with inclination of $\beta = 0°$ (TT0) relative to the orbital plane is considered, so the tether lays exactly on the orbital plane.
3. In the third configuration a tape tether is analysed with an inclination relative to the orbital plane of $\beta = 30°$ (TT30).
4. The fourth configuration consist of a tape tether with $\beta = 60°$ (TT60) of inclination relative to the orbital plane.
5. The fifth configuration has the tape tether inclined by $\beta = 90°$ (TT90) with respect to the orbital plane.

The tape tether can exchange the torsional torque with the space debris and the space tug, while the string tether cannot do that since it does not have any torsional stiffness. This aspect will be relevant in the analysis of the results of cases 2-5.

In every case the tether starts each simulation aligned along the y axis of the LVLH frame.

Six cases of debris initial conditions have been considered and each of them will be evaluated with the five tether conditions. The debris initial conditions are the following:

1. The debris is aligned with the tether and orbits at the same speed of each tether segment and the space tug;
2. The debris is inclined relative to the tether by an angle $\theta = 30°$. This angle is measured between the debris symmetry axis and the tether vector. Since the tether is lays on the y axis of the LVLH frame, the debris rotation is performed around the z axis of the frame in a counter clockwise direction.
3. The debris is inclined relative to the tether by an angle $\theta = 60°$.
4. The debris is aligned ($\theta = 0°$) with the tether and it has an angular rotation of $\omega_2^x = 0.1\frac{rad}{s}$. This case is necessary to evaluate how the tether behaves in case the debris maintains a residual angular momentum after de-tumbling operations.
5. The debris is inclined by an angle $\theta = 30°$ relative to the tether an angular rotation of $\omega_2^x = 0.1\frac{rad}{s}$ is present. This case has the purpose of understanding the tether behaviour in a real situation where de-tumbling operations do not manage to stop all debris' motion and the debris is not aligned with the tether.
6. The debris is aligned ($\theta = 0°$) with the tether and has an initial relative velocity $V_2^x = 0.1\frac{m}{s}$ with respect to the LVLH frame. Tether elements and space tug do not have a relative velocity with respect to the LVLH frame.

The first block of results will be evaluated without the influence of atmospheric drag. In a second time the atmospheric drag will be considered in order to evaluate the influence on the dynamics depending on the tether orientation.

The set of initial conditions is represented in the table below:

$F_y(N)$	-1
$m_1(kg)$	5
$m_2(kg)$	30
$l_0(m)$	100
$l_2(m)$	1
$r_2(m)$	0.25
$\rho_{att}^{'}(m)$	0.5
$width_t(mm)$	10,15,20,25
$thickness_t(mm)$	0.5
$E(GPa)$	110
$\rho_t\left(\frac{kg}{m^3}\right)$	4500
ν_t	0.32
$\alpha_t^p\left(\frac{s}{m}\right)$	0.004
α_t^b	0.08
α_t^t	0.08
Ω	20°
ω	90°
θ	0°
i	60°
e	0.001
$p\ (m)$	6871000

6 RESULTS:

In order to analyse the tether behaviour, it has been necessary to understand which number of segments of the tether should be chosen. To do so, a 100 seconds simulation has been performed with four different number of tether segments: N=10, N=20, N=30, N=40. The N=40 case has been taken as a reference and the other cases' results have been confronted with it. Tether length and deviation angle θ have been calculated for each case. The errors will be calculated relative to the results of the case N=40 at the end of the 100 seconds simulation.

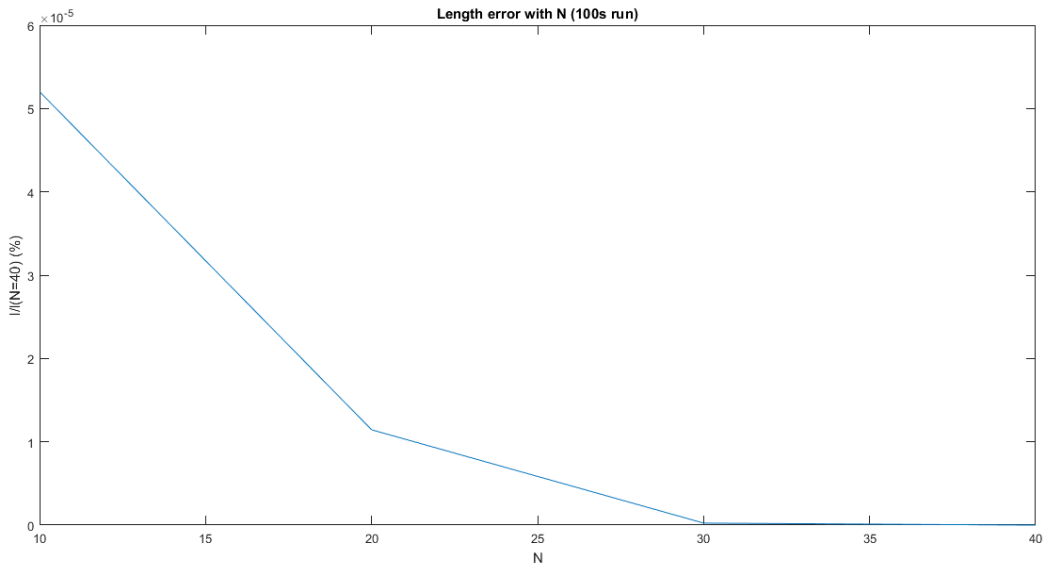

Figure 5: Length error with N

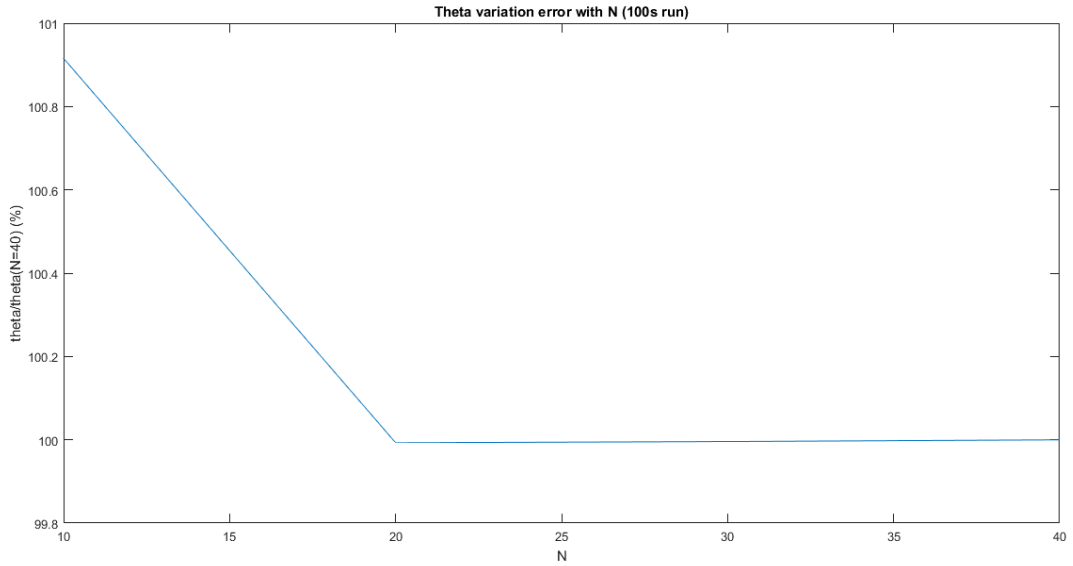

Figure 6: θ error with N

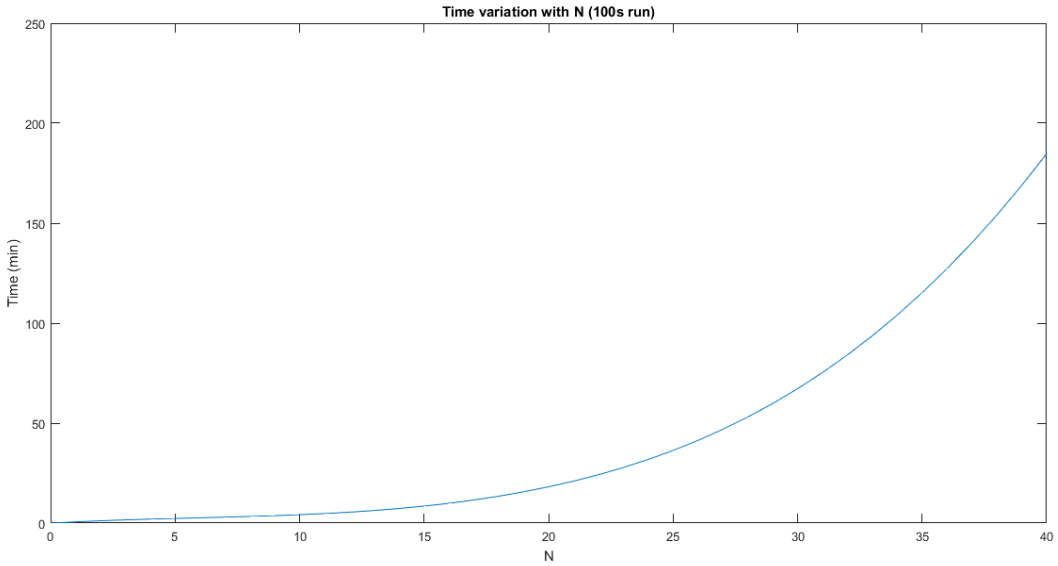

Figure 7: Computing time (minutes) vs N

As we can see from the results the N=10 case requires the least amount of computing time but it has an error of the debris angle θ of about 0.9% at the end of the 100 seconds run. The best choice in terms of results' accuracy would be the case N=40, but the computing time is 185 minutes for a 100 seconds simulation, so it has no practical use. The case N=30 provides results very close to the case N=40, however the computing time is still too high for practical use, since the final simulations will be of 1000 seconds of length. Using a number of segments N=30 in a 1000 seconds simulation results in 11.2 hours of computing time.

The optimum solution is the case N=20, where the computing time is slightly higher than the case N=10 (18.17 minutes vs 4.22 minutes for a 100 seconds simulation) and has an error of 0.01% of the debris angle θ and an error of 0.000015% of the length variation confronted with N=40. For all further analysis a number of segments N=20 will be chosen.

6.1 CASE 1:

For the first case, length variations are not noticeable since the starting conditions are those of the ideal case of a debris perfectly aligned with the tether and without any relative velocity in the LVLH frame. The tether extension is very smooth, thanks also to the damping of the tether.

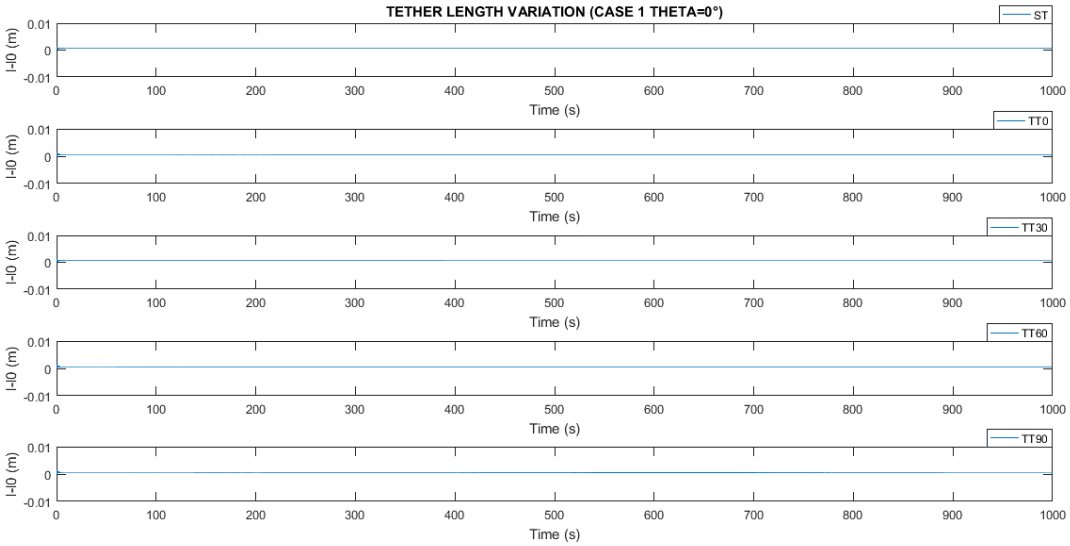

Figure 8: Tether length variation vs time

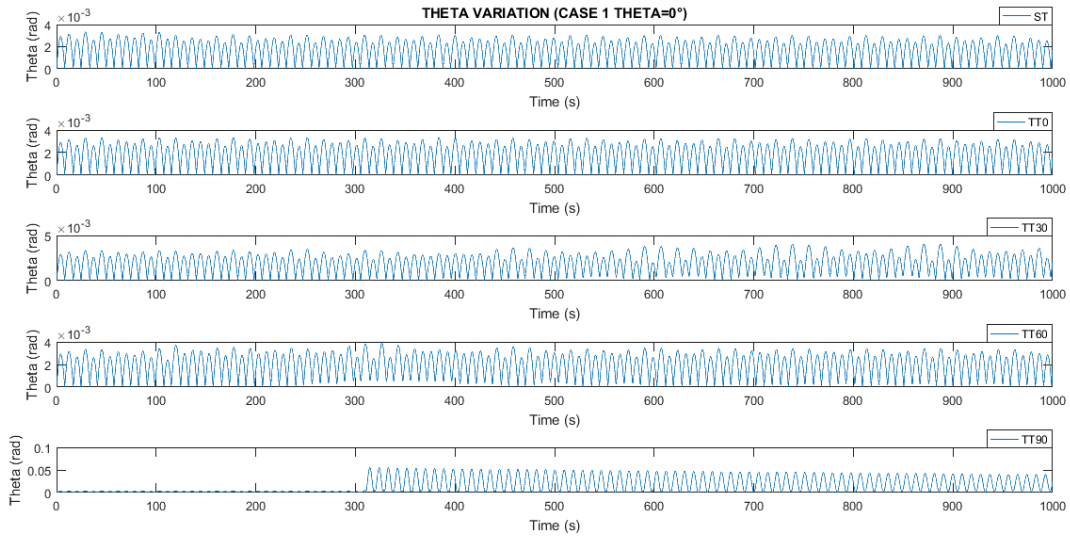

Figure 9: θ vs time

The analysis of the debris' angle θ show a common behaviour of the system in the configurations $\beta = 0°, 60°$ and the string tether configuration, while for the configuration $\beta = 30°$ there is a slightly increase of the oscillations after the 500 seconds mark. It is worth to notice that, in the cases $\beta = 30°, 60°$, it seems that the diagram of the θ variable is provided by the sum of two oscillations, a high frequency one and a low frequency one. This is visible by analysing the minimum values of the oscillations. For the configuration $\beta = 90°$ the oscillations increase by a factor of ten just after the 300 seconds mark, however after that the oscillations

decrease due to the damping effect of the tether. The diagram of the θ peaks and troughs underlines the sudden increase of θ maximum values for the configuration $\beta = 90°$ compared to the other configurations, but also it is evident an increase of the minimum value for the same case compared to the others.

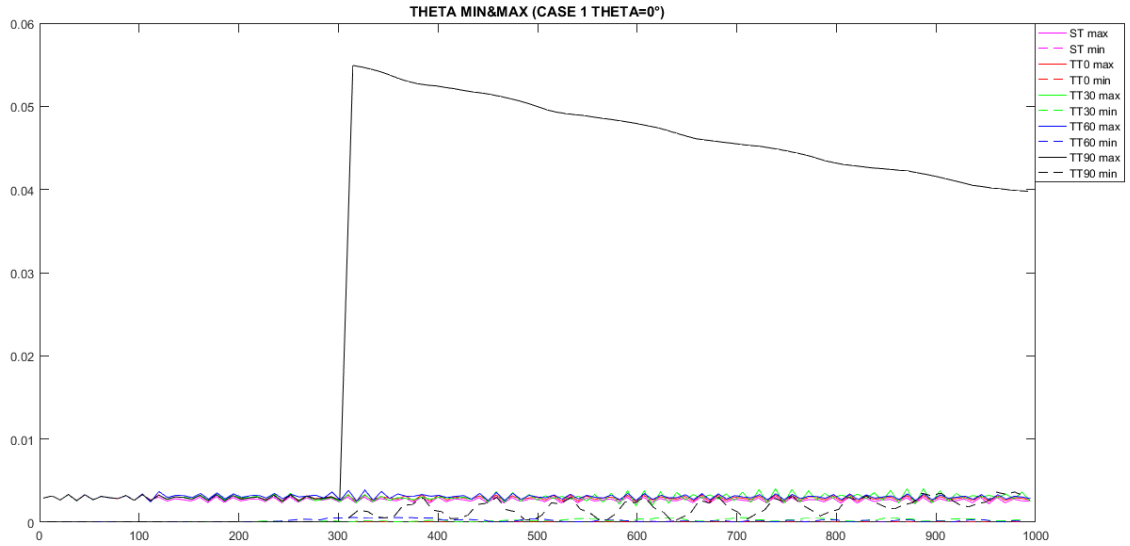

Figure 10: θ maximum and minimum values curves

Another variable of the study is the α angle which is the angle measured between the tether vector and the y axis of the LVLH frame. Such angle is influenced by the gravity gradient torque, however there may be a different pattern due to the configuration of the tether. In figure 11 the pattern of the angle α is similar for every configuration, except for the configuration $\beta = 90°$ which even in this case shows a sudden increase of this variable. It is worth to notice that the α increase occurs in the same time as the θ increase, so there is a correlation between the two events.

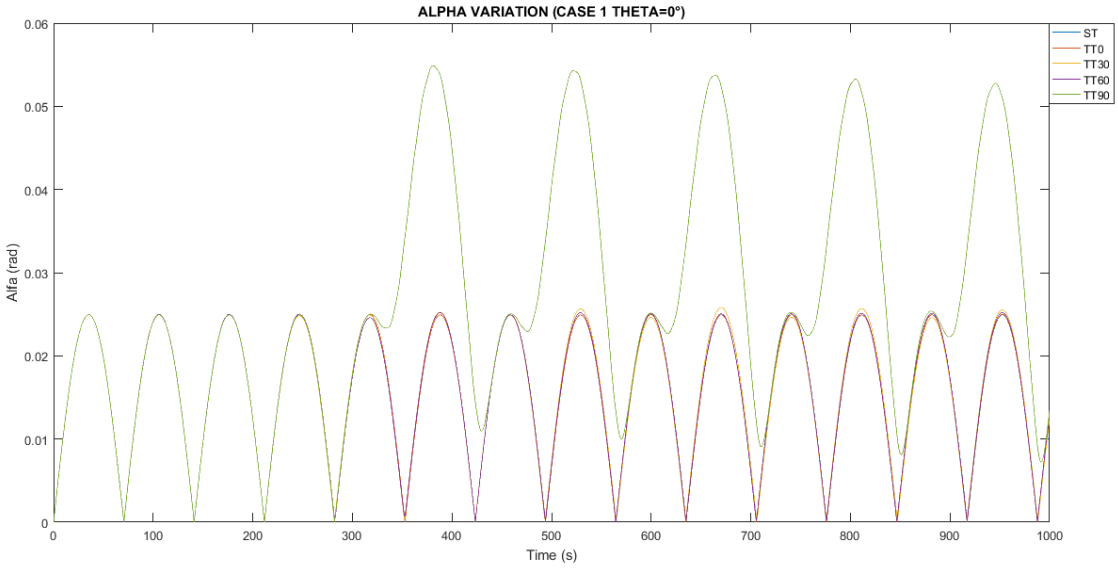

Figure 11: α vs time

6.2 CASE 2:

In this case the starting condition θ=30° causes pendulum-like oscillations in the system for every configuration. The tether's length oscillates with a frequency of about $0.116Hz$ for all configurations.

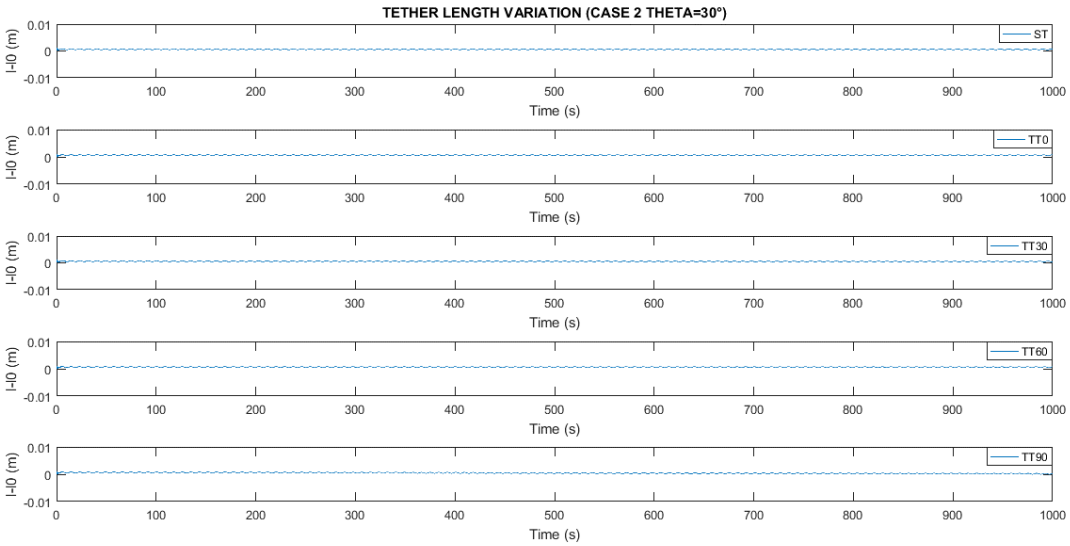

Figure 12: Tether length variation vs time

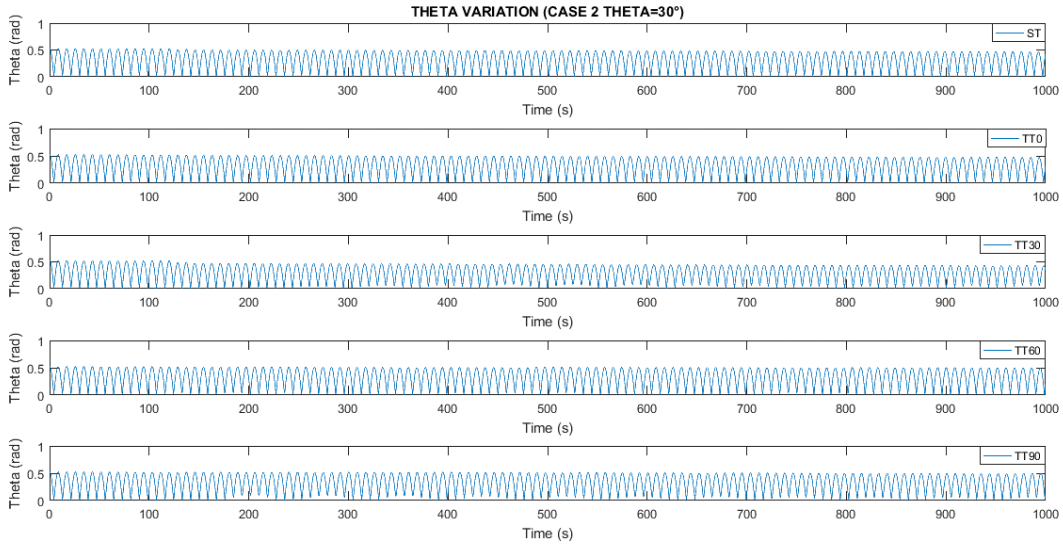

Figure 13: θ vs time

Similar to the tether's length diagrams, θ diagrams show a smooth and regular pattern for every configuration. However in the configuration $\beta = 30°$ there is a slight reduction of θ amplitude just after the 100 seconds mark. For the minimum values the configurations $\beta = 30°, 90°$ show a very slight oscillation with a lower frequency than the main θ oscillation.

In figure 14 it is easier to notice the minimum values oscillations of the cases $\beta = 30°, 90°$ and especially for the case $\beta = 30°$ the θ minimum value peaks follow a very low frequency oscillation. In fact, they reach the maximum value at around 470 seconds and then they fall to a minimum at 820 seconds. From this point on the θ minimum value peaks increase again.

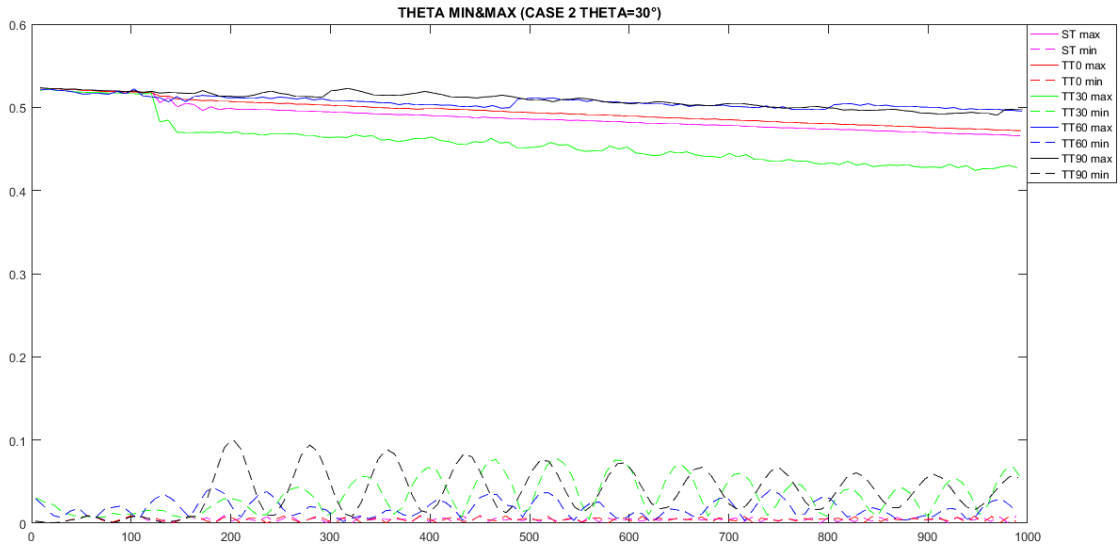

Figure 14: θ maximum and minimum values curves

The distribution of θ peaks shows a clear smooth damping effect in every configuration, with a slight major damping for the case $\beta = 30°$. For this case we can affirm that there is no clear performance advantage for the tape tether compared to the string tether.

Angle α in figure 15 shows about the same patterns for every configuration, except the $\beta = 90°$ one which shows much bigger oscillations compared to the other cases. This effect is due to an oscillating motion of the entire Tether Space System around the x axis of the LVLH frame. During the simulation the α angle for the $\beta = 90°$ configuration shows a slight decrease in amplitude over time after the peak at the 200 seconds mark, but it is not evident whether it is due to a damping effect of the system or to a secondary low frequency oscillation of the variable.

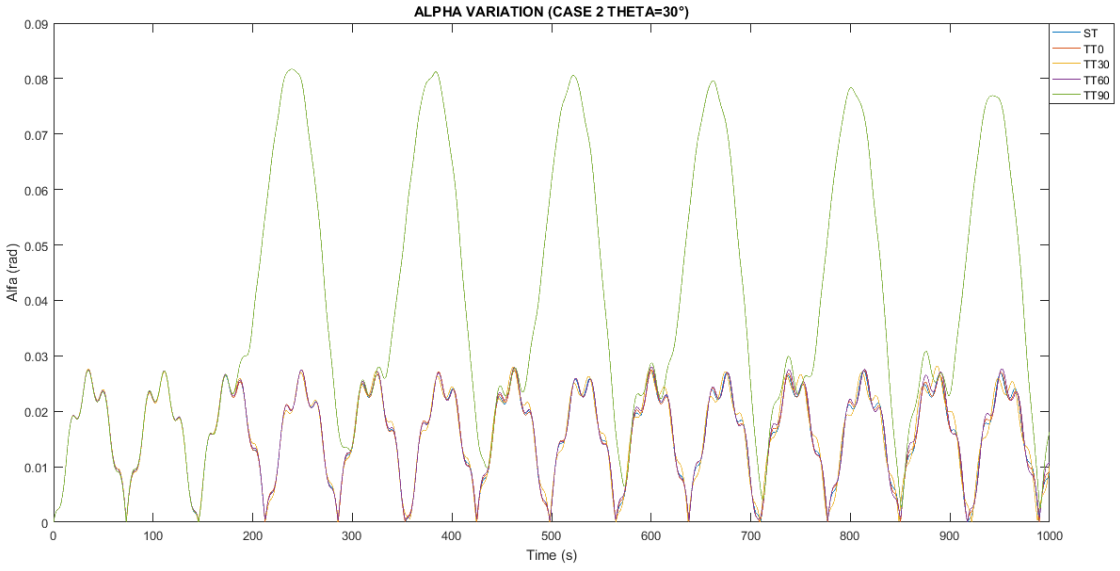

Figure 15: α vs time

6.3 CASE 3:

This case shows tether length variations more irregular compared to the previous case, especially in the configuration $\beta = 30°$. This is related to the higher amplitude of the debris oscillations. Also at the end of the 1000 seconds mark the length variation is negative for the $\beta = 30°$ diagram. This may indicate that the tether is slightly curved.

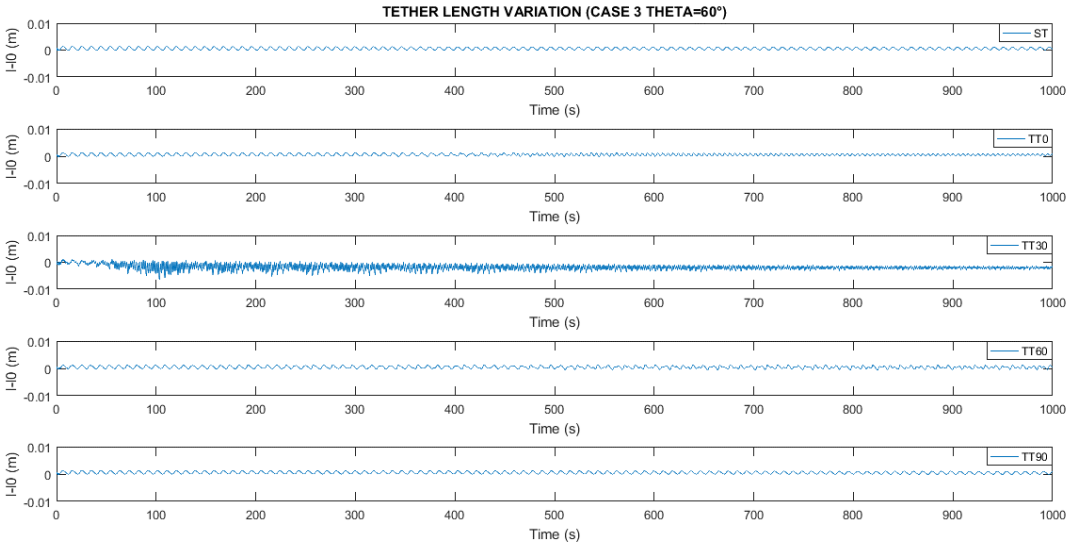

Figure 16: Tether length variation vs time

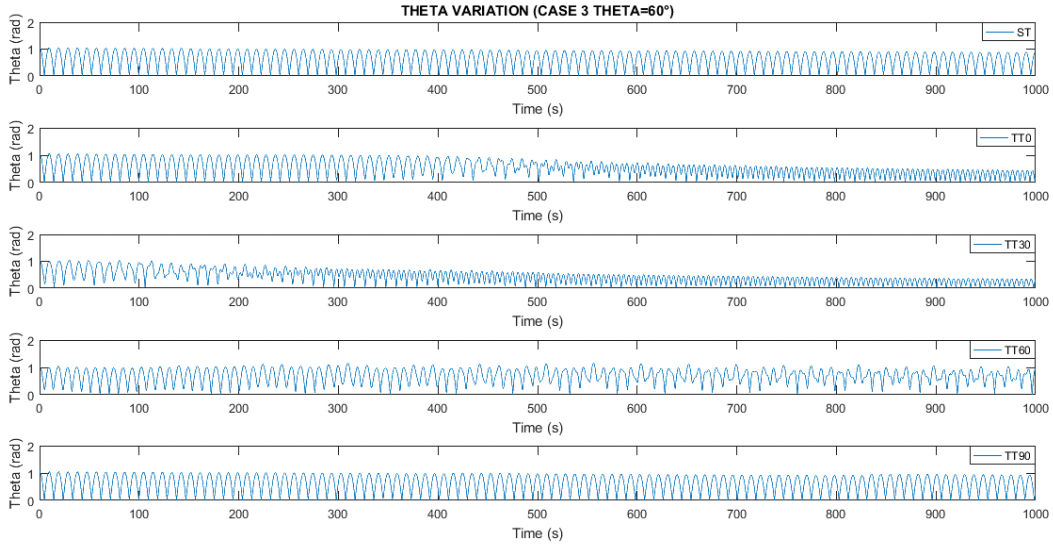

Figure 17: θ vs time

Similar to the length diagrams, θ diagrams show an irregular pattern for the first three tape tether configurations. $\beta = 0°, 30°$ configurations show a particular high damping of the system which is coupled with an increase of the debris oscillation frequency. In both cases it is clear that the θ oscillations face a transition phase from a low frequency to a high frequency pattern. For the case $\beta = 60°$ such transition is not noticeable, but instead

there is an increase of the maximum values and of the minimum values, which in total contribute to the reduction of the total θ oscillations.

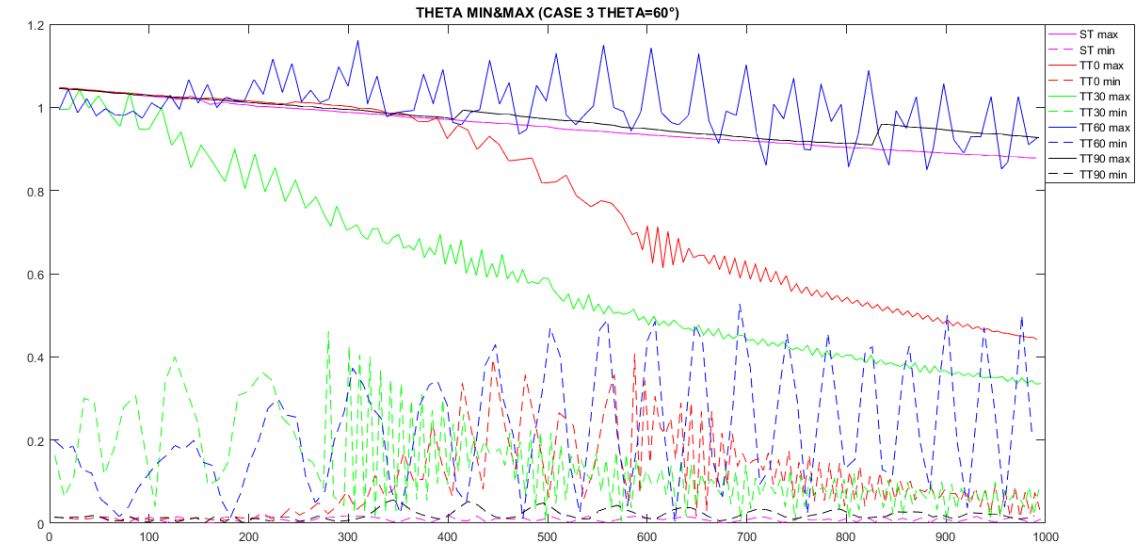

Figure 18: θ maximum and minimum values curves

In figure 18 it is easy to recognise a strong reduction of the oscillations for the cases $\beta = 0°, 30°$ compared to the string tether. The $\beta = 90°$ behaves in a similar way to the string tether, which is expected since the tape tether is bending in the minimum resistance direction, which have the same flexural stiffness of the string tether. The case $\beta = 60°$ is more difficult to analyse since the pattern is not very smooth. In order to overcome this issue, a third degree polynomial fit has been applied to all diagrams (figure 19). From the fit curves it is evident how even in the case $\beta = 60°$ the oscillations are reducing in amplitude.

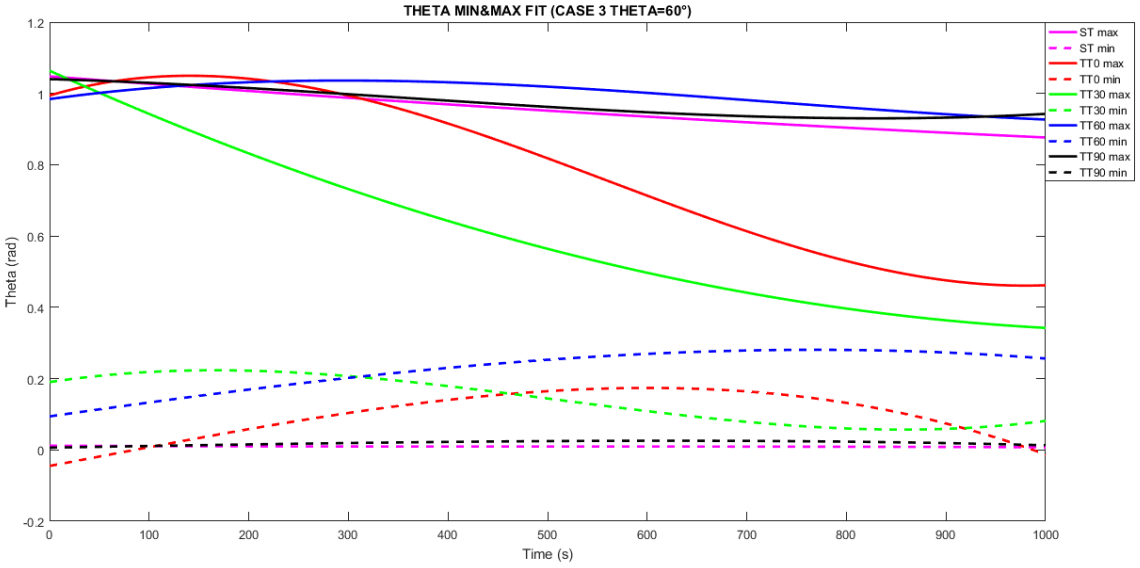

Figure 19: θ maximum and minimum values fit curves

The last parameter, α, shows a more common behaviour compared to the previous cases. In fact the $\beta = 90°$ case doesn't show much difference in amplitude compared to the other cases.

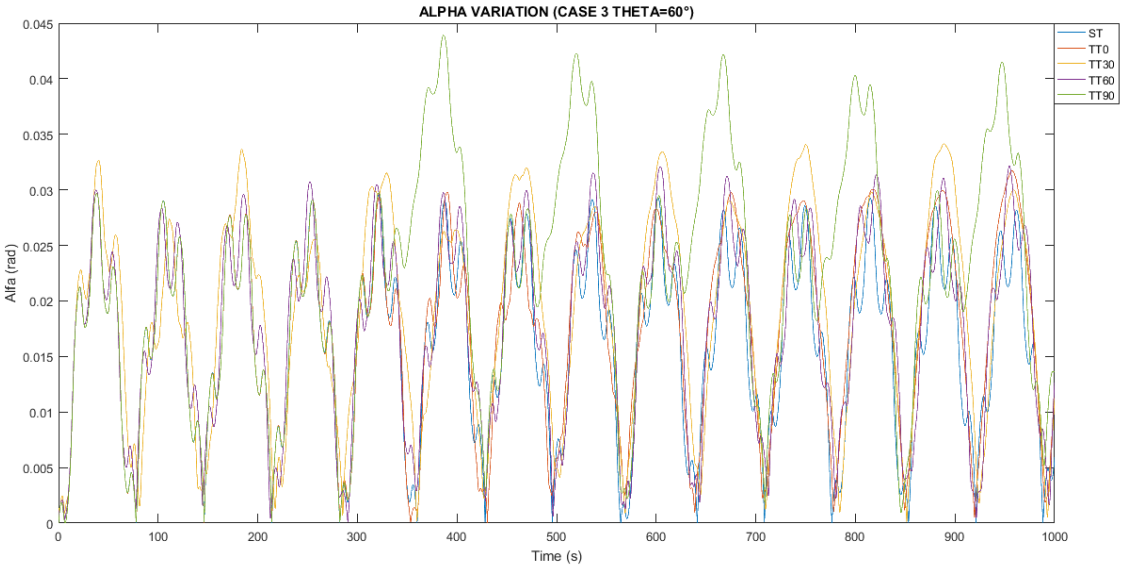

Figure 20: α vs time

6.4 CASE 4:

The purpose of this case is to show the capability of the tape tether to control the roll angle of the debris. As shown in figure 21 the tape tether model provides an overdamped response against the angular motion of the debris, while for the string tether model there is no control over the roll angle. It is possible to notice a strong correlation of the roll angle with the width of the tape tether. This is due to the fact that the torsional stiffness of the tether depends to the cube of the tether's width, so a slightly bigger tether's width results in a strong variation of the roll angle.

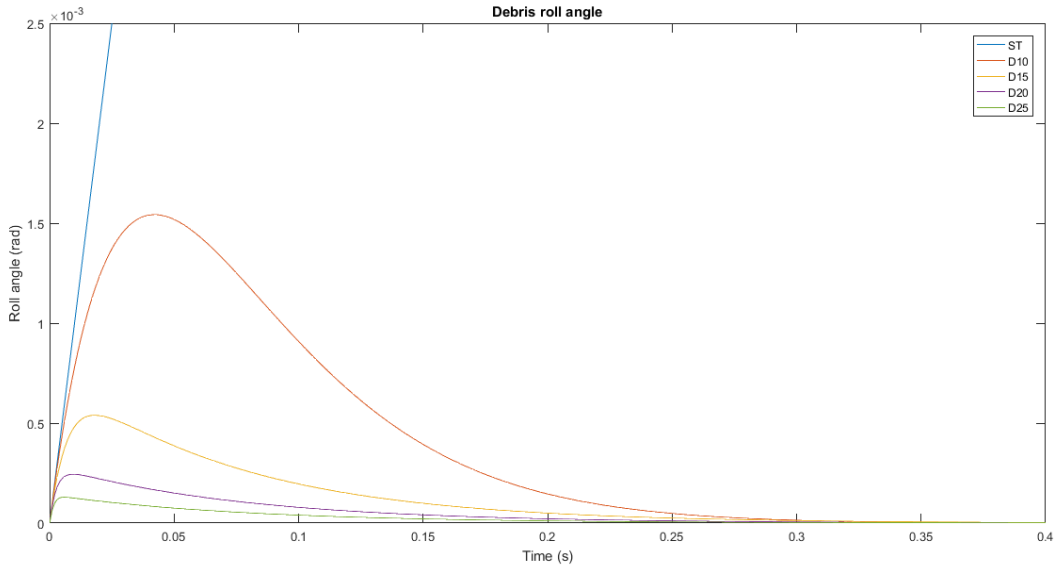

Figure 21: Debris' roll angle vs time

It should be noticed that the tape tether can only control the debris angular momentum up to a certain point until the tether torsional instability occurs. If the instability is reached the tether starts to entangle and the stiffness of the system changes. As result this may lead to the breakup of the tether.

6.5 CASE 5:

In this case the tether length oscillates in a similar fashion to case 2, due to the presence of the initial θ angle. In contrast with the case 3, in this case there are no chaotic oscillations of the tether length.

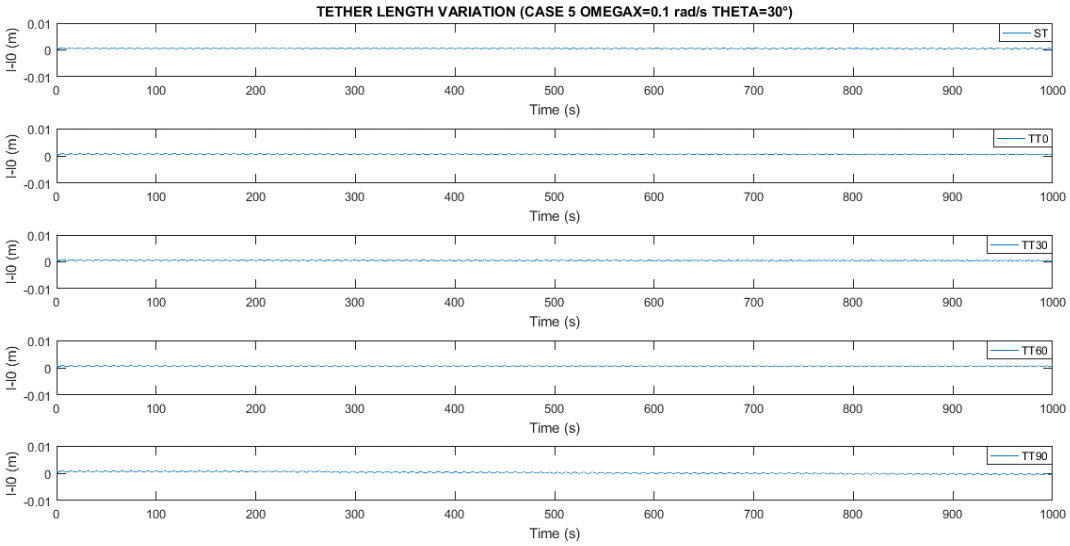

Figure 22: Tether length variation vs time

The angle θ diagrams start with a regular patter for every configuration and then it becomes chaotic. In this case even the string tether configuration reaches such condition. The smoothest configuration is the $\beta = 60°$ which shows a very quick motion damping at the 150 seconds mark. The $\beta = 30°$ shows very high frequency oscillations and a low frequency oscillation of the minimum values. This low frequency oscillation is present also in the configurations $\beta = 0°, 90°$.

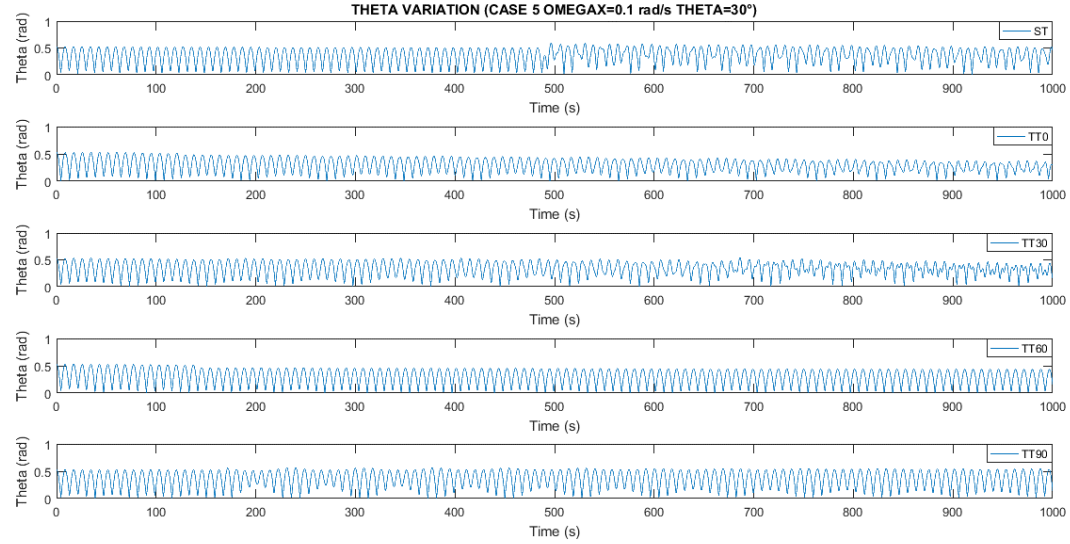

Figure 23: θ vs time

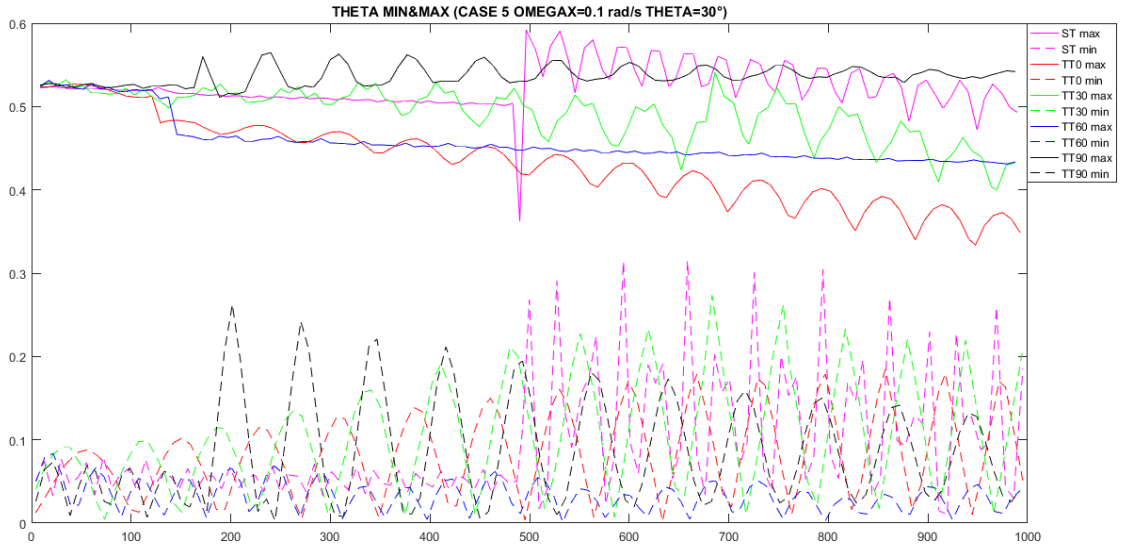

Figure 24: θ maximum and minimum values curves

θ peaks and troughs show a very chaotic pattern for all configurations. It is difficult to clearly quantify the damping for all configurations, since the rapid variations of the θ variable do not allow a precise fit using the MATLAB® polyfit function. However, it is possible to see that all configurations to show a reduction of the amplitude of the oscillations.

The α angle diagram is similar to the case 2, with the same amplitude of all cases, except for the configuration $\beta = 90°$ that has a higher amplitude compared to the other case.

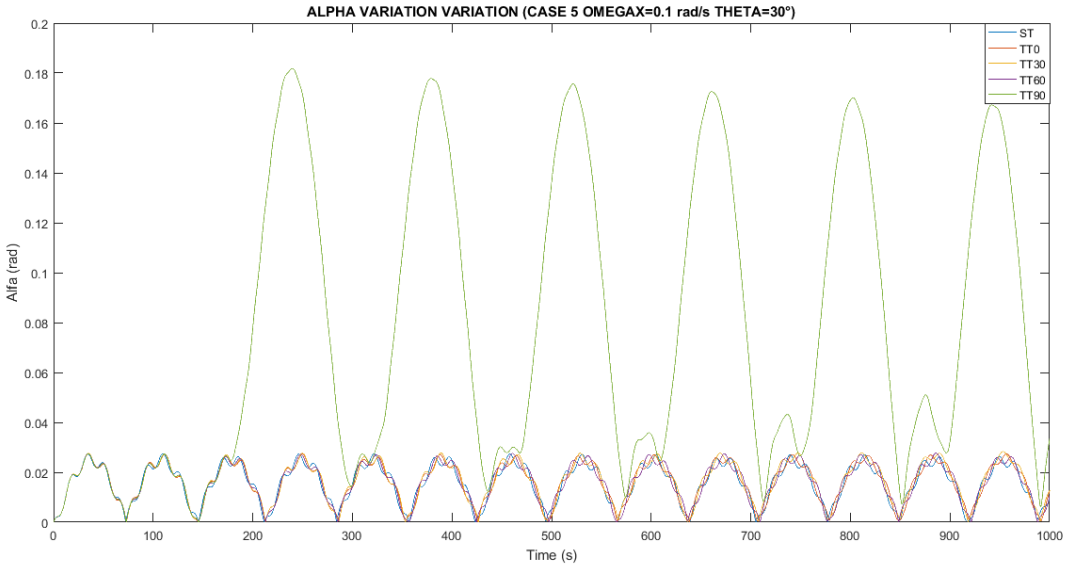

Figure 25: α vs time

6.6 CASE 6:

In this case the length oscillations are very small and quickly damped at the beginning of the simulation. Like in the first case, due to the absence of a starting angle θ, the length variation is approximately constant for each configuration.

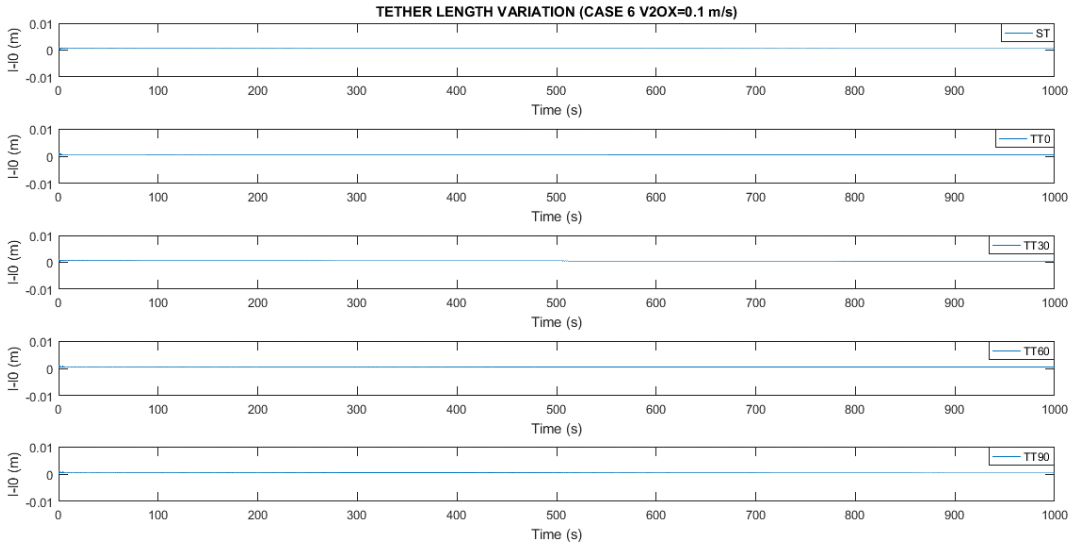

Figure 26: Tether length variation vs time

For the θ diagram is necessary to underline that in every configuration, except $\beta = 90°$, the pattern is quite similar. For the configuration $\beta = 90°$ the θ angle has a low value for the first 30 seconds and then the amplitude increases by a factor of ten.

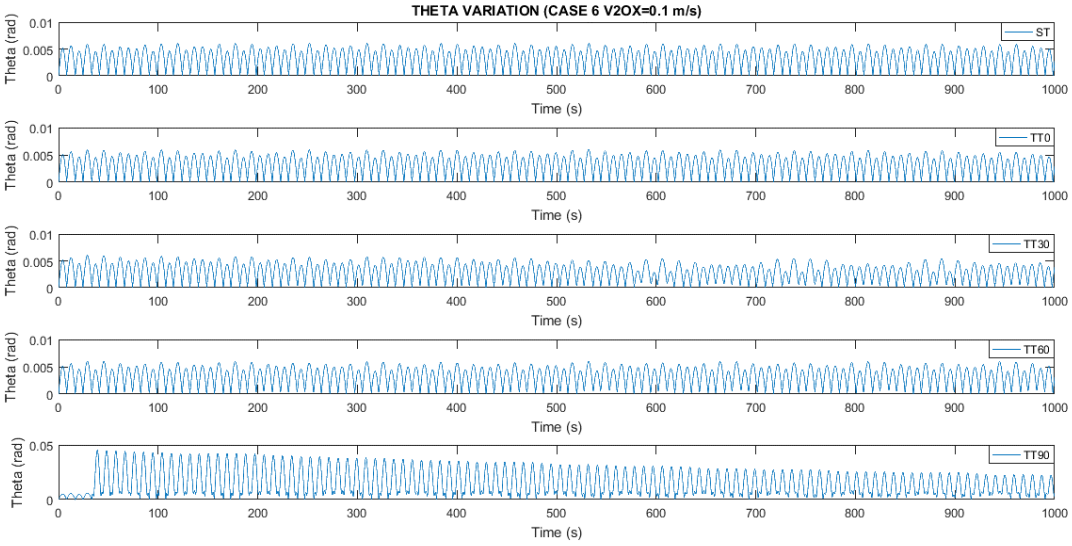

Figure 27: θ vs time

This phenomenon is clearly visible analysing the peaks of the oscillations in figure 28.

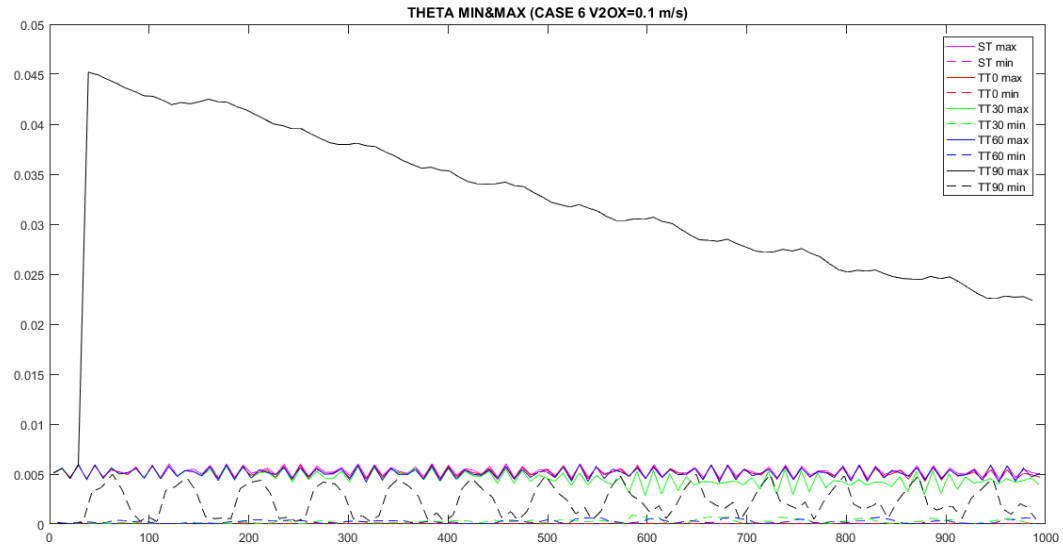

Figure 28: θ peaks

The α diagram shows similarities with the case 1, however in this case the amplitude of the oscillations is higher compared to that case since the starting relative velocity of the debris is not null.

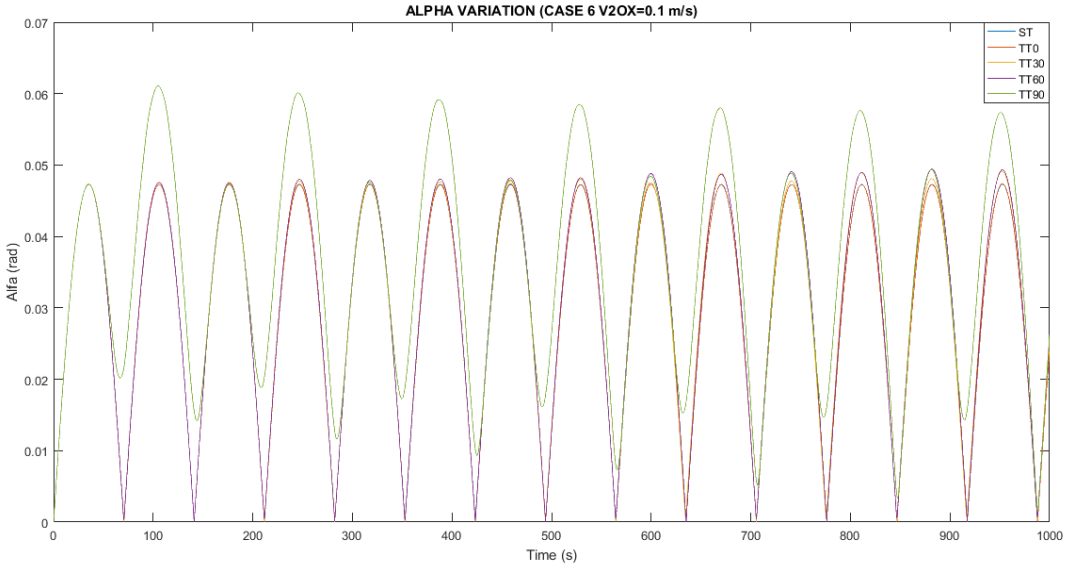

Figure 29: α vs time

6.7 ATMOSPHERIC DRAG EFFECTS:

Until now the dynamics of the TSS has been studied without including the effect of drag. Now the objective is to understand what are the effects of the atmospheric drag on the system. This study has been based on a simple model that does not account for the aerodynamic torques, but it considers only the resulting aerodynamic forces on tether segments, debris and space tug.

Not all results will be shown in this section since some of them do not show any particular feature compared to the "no drag" case, and this time the order of the results will be shown following the variable order instead of the case order.

6.7.1 α variable influence:

The libration angle α has been reduced in amplitude in almost every case compared to the "no drag" cases, especially for the $\beta = 90°$ configuration, while for the other configurations the effect is more subtle. However, the only exception is the case 3 (figure 32) that shows a slight increase of the α variable compared to the no drag case. The effect of the atmospheric drag is clearly visible in almost every case that had a high oscillation of the α variable.

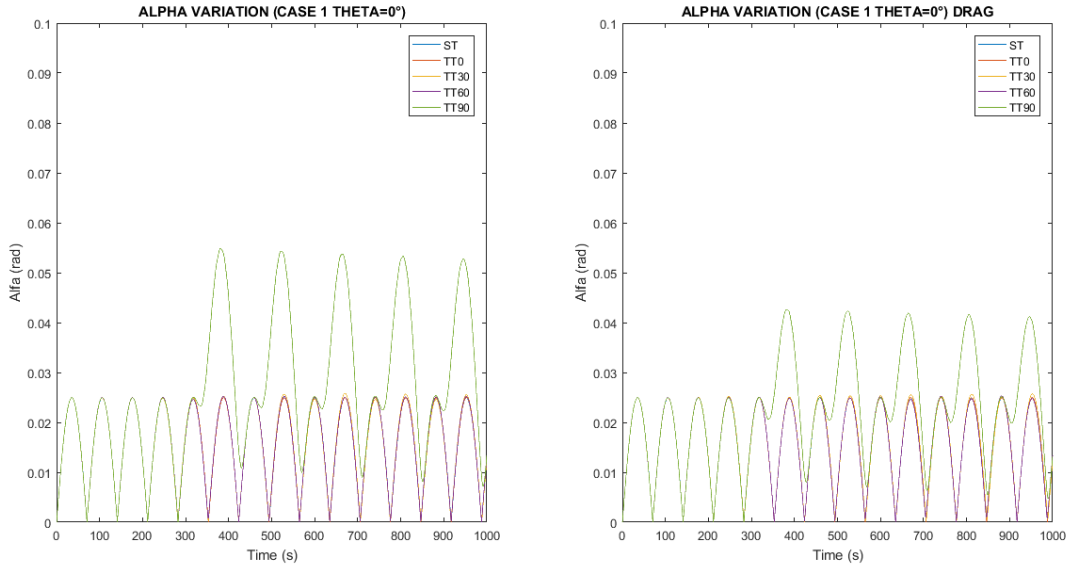

Figure 30: α variable comparison (Case 1)

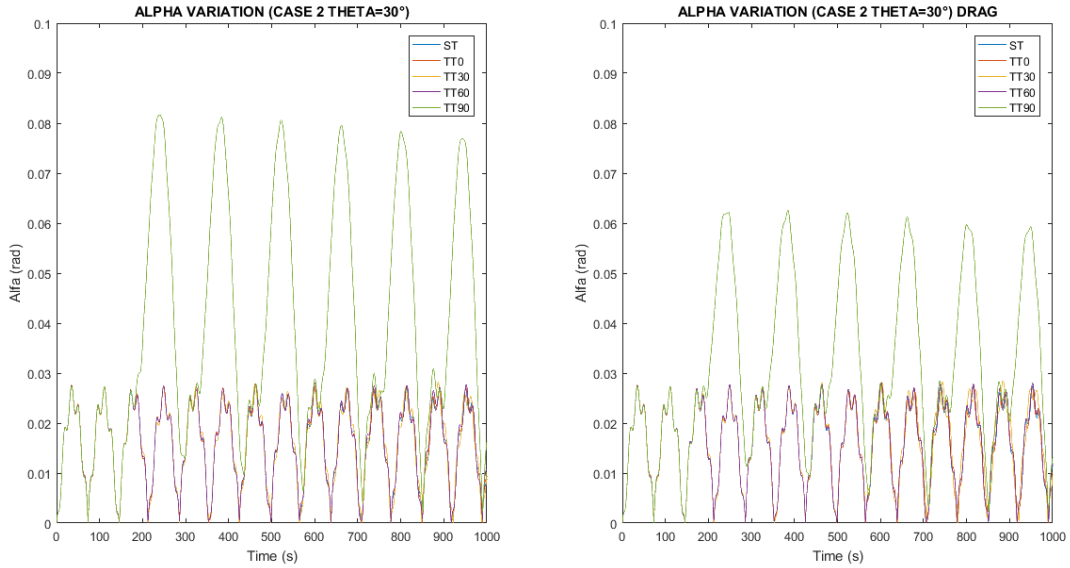

Figure 31: α variable comparison (Case 2)

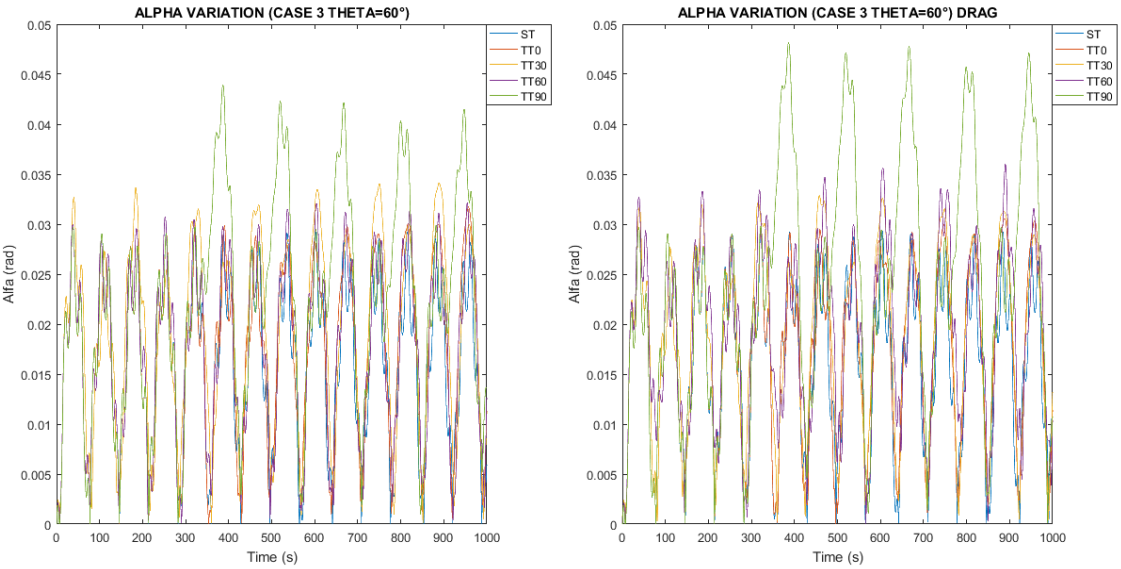

Figure 32: α variable comparison (Case 3)

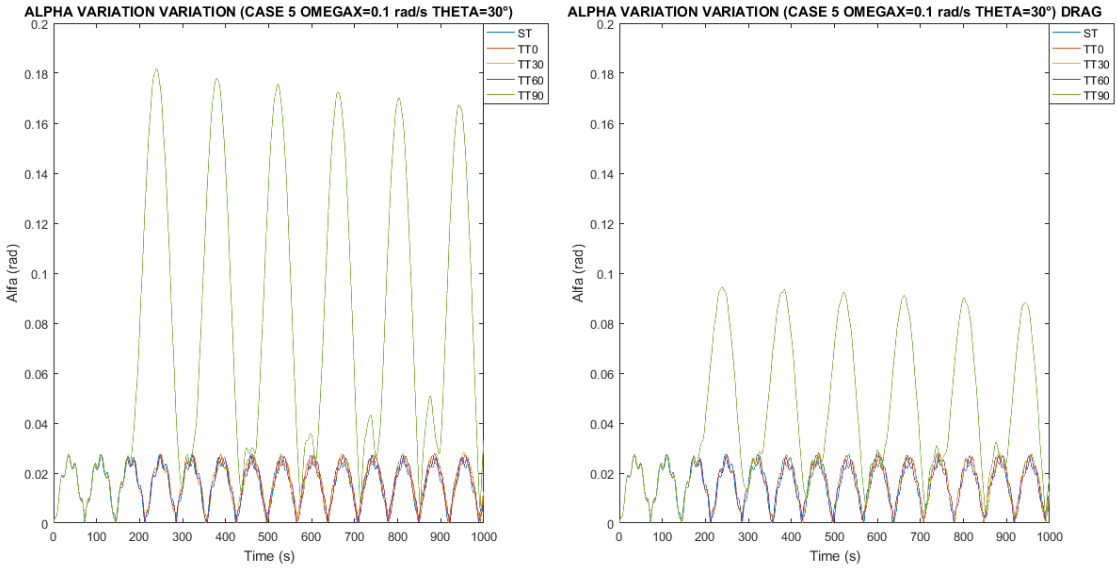

Figure 33: α variable comparison (Case 5)

6.7.2 θ variable influence:

The effect of atmospheric drag on the θ variable is quite contradictory. In the case 2 the effect of drag causes strong oscillations of the θ minimum values and a slight variation of the θ maximum values. In case 3 there is no evident difference between the two cases with or without atmospheric drag, while in the case 5 the atmospheric drag case shows a smoother behaviour compared to the "no drag" case.

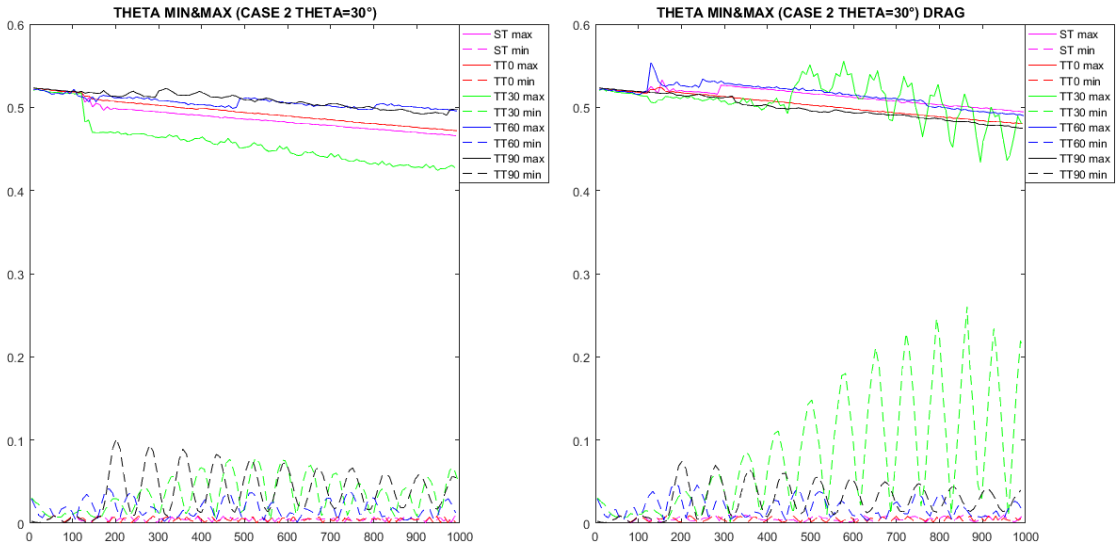

Figure 34: θ diagrams comparison (Case 2)

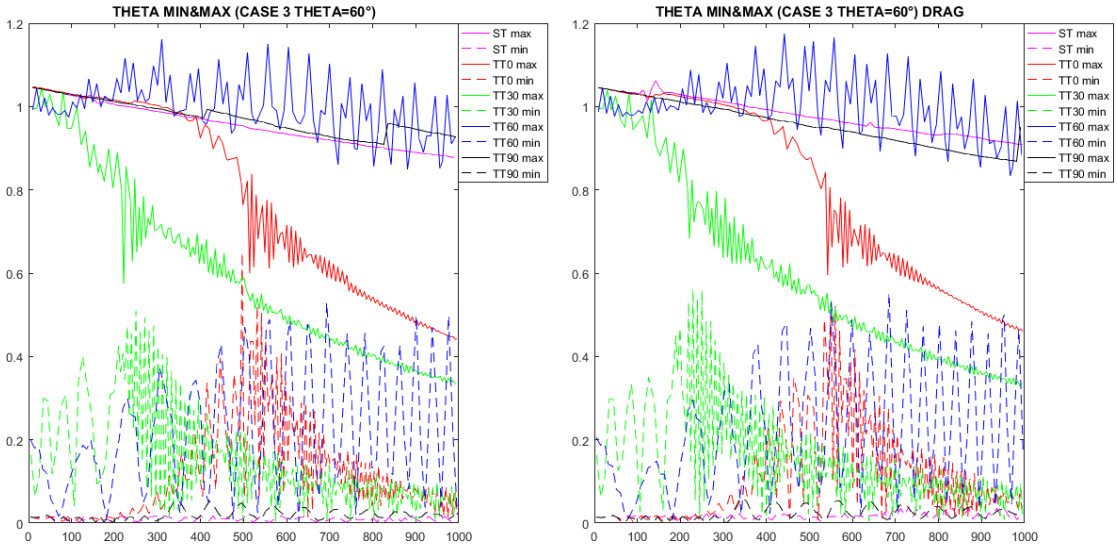

Figure 35: θ diagrams comparison (Case 3)

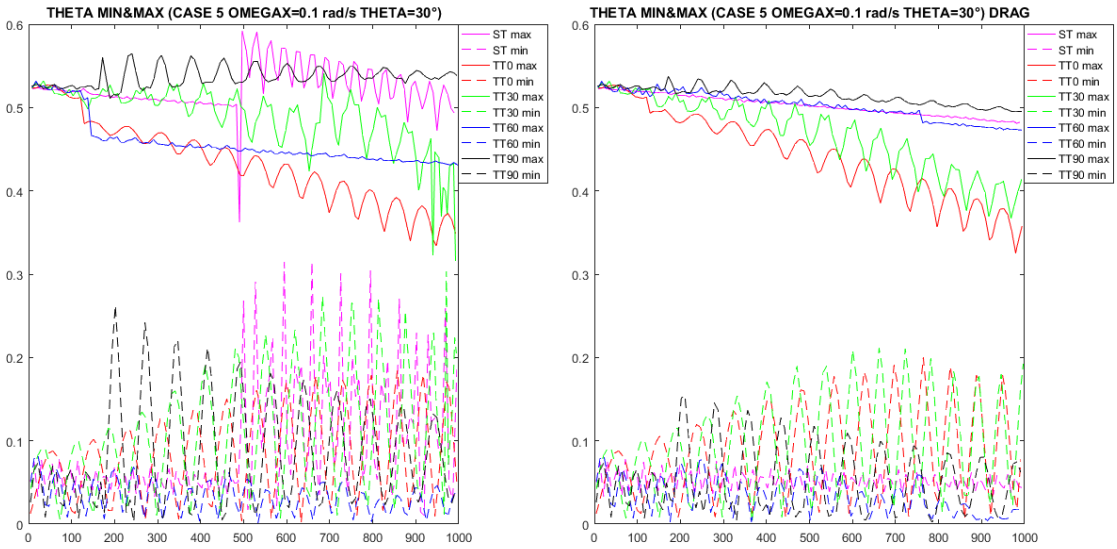

Figure 36: θ diagrams comparison (Case 5)

7 CONCLUSIONS:

In this paper a comparison between the tape tether and the string tether has been made. Different aspects arise from this analysis:

1. The tape tether model has a higher complexity compared to the string tether model in terms of computing time and is necessary to accept a small error in order to have an acceptable computing time;
2. The response of the system with the tape tether depends on the relative inclination β of the tether segments with respect to the orbital plane;
3. For certain element inclinations ($\beta = 90°$ is the main example), the system may develop unpredictable oscillations of the libration angle α;
4. Depending on the configuration of the tape tether, the debris' oscillating motion experiences an increased or similar damping compared to the string tether configuration;
5. The tape tether allows a better control of the debris' roll motion;
6. The presence of atmospheric drag does contribute to a certain extent to the reduction of the libration angle α, but it does not provide any clear advantage over the oscillations of the debris. This aspect has to be better analysed with a more complete aerodynamic model.

8 BIBLIOGRAPHY

[1] ESA, “Space Debris by the Numbers,” [Online]. Available: https://www.esa.int/Our_Activities/Space_Safety/Space_Debris/Space_debris_by_the_numbers.

[2] NASA, “NASA-STD-8719.14A,” NASA, 2011.

[3] NASA, “NASA ODPO's Large Constellation Study,” *Orbital Debris Quarterly News,* vol. 22, September 2018.

[4] ESA, “Active Debris Removal,” [Online]. Available: http://www.esa.int/Our_Activities/Space_Safety/Space_Debris/Active_debris_removal/.

[5] T. W. H. S. H. K. S. T. Y. Y. S. S. T. A. K. T. ,. O. L. J. G. V. K. J. R. S. M. C. M. K. E. J. Hironori A. Fujii, “Space Demonstration of Bare Electrodynamic Tape-Tether Technology on the Sounding Rocket S520-25”.

[6] C. Zhongyi, D. Jingnan and C. Jing, “Hybrid tension control method for tethered satellite systems during large tumbling space debris removal,” *Acta Astronautica,* no. 152, pp. 611-623, 2018.

[7] V. V. Y. Vladimir S. Aslanov, “Chaos in Tethered Tug-Debris System Induced by Attitude Oscillations of Debris,” *Journal of Guidance, Control, and Dynamics.*

[8] S. B. Khan, “Survival Probability of Round and Tape Tethers Against Debris Impact,” *Journal of Spacecraft and Rockets,* 2013.

[9] D. P. J. H. Y. H. Hao Wen, “Advances in dynamics and control of tethered satellite systems,” *Acta Mechanica Sinica,* 2008.

[10] A. A. Shabana, “Computer Implementation of the Absolute Nodal Coordinate Formulation for Flexible Multibody Dynamics,” *Nonlinear Dynamics,* vol. 16, pp. 293-306, 1998.

[11] B. I. J. O. Walker M. J. H., “A set of modified equinoctial orbit elements,” *Celestial Mechanics and Dynamical Astronomy,* vol. 36, pp. 409-419, 1985.

[12] L. Jacchia, “Thermospheric temperature, density and composition. New models.”.

[13] P. D. D. J. B.S. Yu, “Modeling and dynamics of a bare tape-shaped tethered satellite system,” *Aerospace and Science Technology,* vol. 79, pp. 288-296, 2018.